Petroleum Science 21 (2024) 4464–4480

Contents lists available at ScienceDirect

Petroleum Science

journal homepage: www.keaipublishing.com/en/journals/petroleum-science

Original Paper

Unraveling the corrosion behavior and corrosion scale evolution of N80 steel in high-temperature CO_2 environment: The role of flow regimes

Liu-Yang Yang [a, b], Chang-Pu Liu [a, b], Hai-Ming Fan [a, b, *], Da-Lei Zhang [a, c], Zhi-Yi Wei [a, b], Hui-Liang Wu [a, b], Chuan He [a, c], Ye-Fei Wang [a, b]

[a] State Key Laboratory of Deep Oil and Gas, China University of Petroleum (East China), Qingdao, 266580, Shandong, China
[b] Shandong Key Laboratory of Oilfield Chemistry, School of Petroleum Engineering, China University of Petroleum (East China), Qingdao, 266580, Shandong, China
[c] School of Materials Science and Engineering, China University of Petroleum (East China), Qingdao, 266580, Shandong, China

ARTICLE INFO

Article history:
Received 2 July 2024
Received in revised form
26 August 2024
Accepted 3 November 2024
Available online 5 November 2024

Edited by Min Li

Keywords:
CO_2 corrosion
Oil well tubing
High temperature and high pressure
Corrosion scale
Flow regimes

ABSTRACT

During CO_2 transportation and storage, metal equipment such as oilfield pipelines suffers from severe CO_2 corrosion, especially in harsh downhole injection equipment. In this study, we investigated the corrosion behavior of oil well tubing in a high-temperature, high-pressure (HTHP) CO_2-containing environment. The evolution of the corrosion scale was also examined under different flow regimes. The results reveal a lower corrosion rate at 150 °C compared to 80 °C under different flow regimes, with localized corrosion intensifying as temperature and rotational speeds (v_{rs}) increase. The temperature also induces the corrosion scale conversion of aragonite-type $CaCO_3$ (80 °C) to calcite-type $CaCO_3$ (150 °C). Specifically, the variation of the corrosion rate and the corrosion scale evolution can be attributed to the vortices within the reactor. The intact vortex cells enhance mass transfer while also promoting nucleation and growth of $CaCO_3$. However, when v_{rs} exceeds the critical Reynolds number, the vortex cells are disrupted, resulting in viscous dissipation and a reduced corrosion rate.

1. Introduction

The pursuit of low-carbon green development strategies necessitates the adoption of key technologies aimed at substantial reductions in carbon emissions. One such technology is carbon capture, utilization and storage (CCUS), which has attracted widespread attention from various industries around the world (Ishaq and Crawford, 2023; Wang et al., 2023). The use of CO_2-enhanced oil recovery (CO_2-EOR) technology for CCUS represents a win-win strategy as it involves both carbon storage and utilization (Li and Zhang, 2011; Azzolina et al., 2015, 2016; Davoodi et al., 2023). However, as the exploitation of deep unconventional oil and gas reservoirs progresses into increasingly extreme conditions, the issue of CO_2 corrosion in oil well tubing has become increasingly severe (Li et al., 2019; Alaba et al., 2020; Chen et al., 2021; Yang et al., 2024). Investigating the corrosion behavior of deep-well tubing is of paramount importance for ensuring the safe and stable operation of the energy industry.

The oil well tubing is the main flow channel during oil injection and recovery processes (Yan et al., 2023). The CO_2-induced corrosion of oil well tubing involves the complex interaction of flow, electrochemical, and mass transfer processes (Bénézeth et al., 2009; Alsaiari et al., 2010a; Esmaeely et al., 2013; Hua et al., 2018). Two central issues in oil well tubing corrosion under flowing regimes are the mass transfer of corrosive media and corrosion scale deposition (Marosek et al., 1993; Gao et al., 2011; Hua et al., 2018; Yue et al., 2020; Wang et al., 2022b; Zhao et al., 2022). It is well known that dense $FeCO_3$ scale can block the active sites on carbon steel, preventing the diffusion of electrochemically active substances (Nešsić, 2006; Ruzic et al., 2006; Ren et al., 2021; Wang

* Corresponding author. Shandong Key Laboratory of Oilfield Chemistry, School of Petroleum Engineering, China University of Petroleum (East China), Qingdao, 266580, Shandong, China
E-mail address: haimingfan@126.com (H.-M. Fan).

https://doi.org/10.1016/j.petsci.2024.11.002

Nomenclature

v_{corr}	average corrosion rate, mm/a;
v_{rs}	rotational speed, rpm;
Re	Reynolds number;
$Re_{,c}$	critical rotational Reynolds number;
ρ	fluid density, kg/m^3;
N	rotational speed of the blade, r/s;
D	blade diameter, 0.052 m;
μ	dynamic viscosity of the fluid, Pa·s;
m_0	steel weight before corrosion, g;
m_1	steel weight after corrosion, g;
S	total area of the steel sheet, cm^2
ρ_s	density of the steel sheet, g/cm^3
t	period of the corrosion experiment, h;
v_{pr}	pitting rate, mm/a;
h_{max}	deepest pitting depth, mm;
T_{pr}	exposure time, day (d);
S_{FeCO_3}	supersaturation of $FeCO_3$;
S_{CaCO_3}	supersaturation of $CaCO_3$;
$K_{sp,FeCO_3}$	solubility constants of $FeCO_3$;
$K_{sp,CaCO_3}$	solubility constants of $CaCO_3$;
T_K	temperature in Kelvin, K;
k	turbulent kinetic energy, m^2/s^2;
ε	turbulent dissipation rate, m^2/s^3;
τ_w	wall shear stress, Pa;
v	fluid in line velocity, m/s;
P_g	partial pressure of CO_2;
K_H	Henry constant;
C	CO_2 fraction;
f	Fanning friction coefficient;
D_i	diffusion coefficient, m^2/s;
$D_{i,T}$	turbulent diffusion coefficient, m^2/s;
C_{mu}	empirical constant;
l_μ	turbulent length scale;
S_c	Schmidt number, dimensionless;
$S_{c,T}$	turbulent Schmidt number;
y^+	distance from the substrate, mm;
κ	von Karman constant;
C_μ	constant for turbulence modeling;
C_i	concentration at a distance y+ from the wall, mol/L;
$C_{i,w}$	concentration on the substrate;
$J_{i,w}$	diffusive flux in the near-wall region;
∇Y_i	mass fraction of corrosive medium;
$\mu_{T,layer}$	turbulent viscosity, Pa·s;
ε	turbulent dissipation rate, m^2/s^3;

et al., 2022b; Owen et al., 2023). Moreover, it is generally assumed that flow velocity inhibits or retards the nucleation and growth of $FeCO_3$ under the NaCl system (Yue et al., 2020; Wang et al., 2022a). Han et al. (2009) demonstrated that high flow velocities can cause the failure of corrosion scales on sample surfaces in CO_2 aqueous solutions, and the formation of a potential difference under the corrosion scale can propagate localized corrosion. Elgaddafi et al. (2021) using the Couette flow device, the wall shear stress from rotating flow at 38 °C was found to lead to mass transfer enhancement and sweet corrosion acceleration, while high temperature (71 °C) flow favored protective scaling and pitting. However, no consensus has been drawn on the corrosion behavior and corrosion scale distribution under different flow regimes, including laminar to turbulent flow evolution.

In addition, massive of metal cations, such as Ca^{2+}, are present in the produced oilfield fluids of highly mineralized oilfield formations. Ca^{2+} not only affects the solubility of CO_2 in the aqueous phase, but also reacts with dissolved CO_2 to form mineral scales such as calcium carbonate ($CaCO_3$) and mixed carbonate ($Fe_xCa_yCO_3$) (Chen et al., 2023). Specifically, Alsaiari et al., 2010b found that Ca^{2+} is essential for improving the solubility of $FeCO_3$, thereby avoiding the sedimentation of solid $FeCO_3$. Esmaeely et al. (2013) and Navabzadeh et al. (2016) studied the corrosion electrochemical behavior under a wide range of Ca^{2+} concentrations, revealing that a protective layer can still form at low Ca^{2+} concentrations (up to 100 ppm), thereby reducing the corrosion rate (v_{corr}). By contrast, $CaCO_3$ and $Ca_xFe_yCO_3$ layers formed at higher Ca^{2+} concentrations (1000 ppm and 10000 ppm) were unprotective and inhomogeneous, resulting in the increased v_{corr}. Also, the increase in Ca^{2+} concentration facilitates the propagation of pits, but reduces the v_{corr} (Hua et al., 2018). The formation and propagation of pits is significantly faster at 150 °C than at 80 °C (Shamsa et al., 2019). However, the corrosion scale evolution of oil well tubing in high mineralization systems under flow regimes is not clear.

The present study aims to address the identified gaps in the literature by investigating the corrosion behavior and the mechanism of corrosion scale evaluation in N80 steel under different flow regimes. Based on this, laboratory-scale High temperature and High pressure (HTHP) reactors were used to simulate the environments in deep oil and gas wells. The mechanism of corrosion scale formation was elucidated by characterizing the corrosion morphology and composition. Furthermore, computational fluid dynamics (CFD) were conducted using Ansys Fluent to characterize the vortex distribution inside the reactor at different rotational speeds (v_{rs}).

2. Experimental

2.1. High-temperature and high-pressure corrosion weight loss experiment

N80 steel with a size of 50 × 10 × 3 mm was selected for HTHP corrosion weight loss experiments to obtain the v_{corr}. The composition (wt.%) of N80 steel is 0.31% C, 0.26% Si, 1.32% Mn, 0.036 Cr, 0.021 Mo, 0.033% Ni, 0.017% Al, 0.003% P, and Fe balanced. Before the experiment, the surface of N80 steel was polished to 1200 # with silica carbonized sandpaper, followed by rinsing with ethanol, and deionized (DI) water. In the HTHP corrosion weight loss experiments, four N80 steel samples were selected for parallel tests, and the test period was 48 h. The working diagram of the HTHP reactor is shown in Fig. 1.

The aqueous phase used in experiments was prepared with reference to a typical formation fluid extracted in the northwest of China, with a $CaCl_2$ water type. The specific brine composition is shown in Table 1. N_2 was bubbled through the aqueous phase to ensure that its dissolved oxygen content was less than 20 ppb. Prior to the HTHP corrosion tests, the N80 steel samples were secured to the sample holder, which were made of PEEK to avoid galvanic corrosion. The experimental testing regimes are shown in Table 2. Two different experimental temperatures (80 °C and 150 °C) were selected, while the total experimental pressure was maintained at 4 MPa and the partial pressure of CO_2 was set at 2 MPa. To investigate the corrosion behavior under static, laminar, and turbulent flow regimes, six rotational speeds were set, with the Reynolds number (Re) used to characterize the flow regime.

The calculation equation of Re is shown in Eq. (1), and the linear velocity of the fluid in the actual water injection pipeline is calculated based on Eq. (2). The calculated changes in Re at different rotational speeds are shown in Table 2. The criteria for determining the flow regime based on Re are shown in Table 3.

$$Re = \frac{\rho \cdot N \cdot D^2}{\mu} \tag{1}$$

$$v = \pi D \cdot N \tag{2}$$

where ρ is the density of the fluid, kg/m^3; N is the rotational speed of the blade, r/s; D is the diameter of the blade, which is 0.052 m;

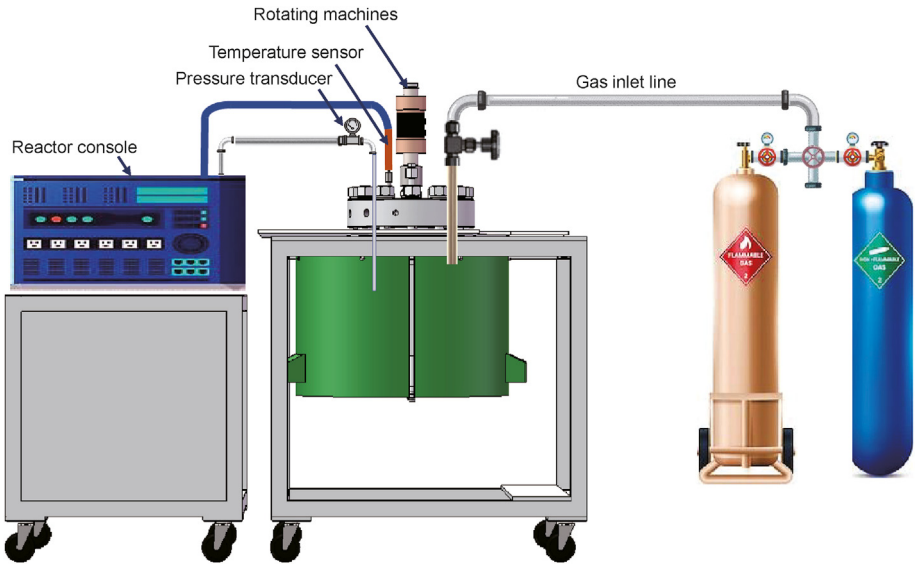

Fig. 1. HTHP reactor working diagram.

Table 1
Composition of extraction fluids from a formation in an oil field.

Ion	$Na^+ + K^+$	Ca^{2+}	Cl^-	SO_4^{2-}	Mg^{2+}	HCO_3^-	Total mineralization
Concentration, mg/L	11547.23	29559.1	75525.09	500	138.39	250.87	111977.3

Table 2
Fluid parameters at different temperatures and Re changes at different speeds.

T, °C	Impeller rotation speed, rpm	Impeller diameter, mm	Liquid density, kg/m^3	Liquid viscosity, Pa•s	Reynolds number
80	0	52	1032.40	3.72×10^{-4}	/
	10 (0.03 m/s)				1250.72
	150 (0.41 m/s)				18760.82
	300 (0.82 m/s)				37521.63
	400 (1.09 m/s)				50028.84
	500 (1.36 m/s)				62536.06
	660 (1.79 m/s)				82547.59
150	0		913.60	1.94×10^{-4}	/
	10 (0.03 m/s)				2122.31
	150 (0.41 m/s)				31834.72
	300 (0.82 m/s)				63669.44
	400 (1.09 m/s)				84892.59
	500 (1.36 m/s)				106115.74
	660 (1.79 m/s)				140072.78

Table 3
The relationship between *Re* and flow regime.

Flow regime	Laminar	Transition state	Turbulence
Re	<2300	2300–4000	>4000

and μ is the dynamic viscosity of the fluid. After the experiment, the N80 samples were placed in an acid wash solution to remove the surface corrosion scales. The ratio of the acid wash solution is configured in accordance with GB/T16545-2015. The mass loss due to corrosion is calculated using Eq. (3).

$$v_{corr} = \frac{87600 \times (m_0 - m_1)}{S \cdot t \cdot \rho_s} \quad (3)$$

where v_{corr} is the average corrosion rate, mm/a; m_0 and m_1 are the weight of the steel sheet before and after corrosion experiment, respectively, g; S is the total area of the steel sheet, cm^2; ρ_s is the density of the steel sheet, g/cm^3; t is the period of the corrosion experiment, h.

2.2. Surface morphology analysis

The corrosion morphology and compactness of the corrosion scale under different flow regimes were evaluated using the American FEI Quanta FEG250 field emission scanning electron microscope (SEM). The corrosion morphologies were taken at an acceleration voltage of 8 kV and an approximate working distance of 8 mm. In addition, combine the observations of cross-sectional morphology and energy-dispersive X-ray spectroscopy (EDS) testing (Oxford IncaEnergy X-max-50 X-ray energy spectrometer, Oxford, UK) for corrosion scale composition testing.

The composition of the corrosion scale was characterized using the Nihon Riken SmartLab X-ray diffractometer (XRD), employing Cu Kα radiation and a diffraction slit with an effective area of 10 × 10 mm. Scanning was performed with a step size of 0.1667 per second in the range of $2\theta = 20°–70°$.

Additionally, the microscopic contours of the pitting pits after descaling was observed using a laser 3D profilometer (VHX-7000 N), and the maximum depth of pits (h_{max}) was measured in μm. The maximum pitting rate was calculated using Eq. (4) with units in millimeters per year (mm/a).

$$v_{pr} = \frac{h_{max} \cdot 0.001 \cdot 365}{T_{pr}} \tag{4}$$

Where v_{pr} is the pitting rate, mm/a; h_{max} is the deepest pitting depth, mm, and T_{pr} is the exposure time, day (d).

2.3. CFD simulation

The three-dimensional model of the rotating reactor used in the numerical simulations (Fig. 2(a)) was drawn using AUTOCAD software, and includes the kettle body, paddles, N80 steel hangers, and grippers. Ansys Fluent was used for meshing and rotating mechanical flow simulation. The mesh size was set to 0.5 mm and the size function was set to Curvative. The Reynolds-averaged Navier-Stokes equation was used to simulate the flow at different rotational speeds. The density and viscosity of the solution at different temperatures during the simulation were set based on Table 2. The no-slip boundary condition was applied at the wall surface, and the mass and momentum transfer in the fluid phase were described using the RNG k-ε model as follows (Speziale and Thangam, 1992; Shih et al., 1995; Balestrin et al., 2021):

$$(\overline{v}) = 0 \tag{5}$$

$$\nabla \cdot (\rho\overline{v}\overline{v} + \rho\overline{v'v'}) = -\nabla\overline{p} - \nabla \cdot \overline{\tau} + \rho g \tag{6}$$

$$\overline{\tau} = \mu\left(\nabla\overline{v} + \nabla\overline{v}^T\right) - \frac{2}{3}\mu\nabla\cdot\overline{v}I \tag{7}$$

The k and ε turbulence equations in the RNG k-ε model are explained as follows (Speziale and Thangam, 1992; Shih et al., 1995).

$$\frac{\partial(\rho k)}{\partial t} + \nabla\rho k u_i = \nabla\left(\alpha_k u_{eff}\nabla k\right) + G_k + G_b - \rho\varepsilon - Y_M + S_k \tag{8}$$

$$\frac{\partial(\rho\varepsilon)}{\partial t} + \nabla\cdot(\rho\varepsilon v) = \nabla\cdot\left(\alpha_\varepsilon\mu_{eff}\nabla\varepsilon\right) + C_{1\varepsilon}\frac{\varepsilon}{k}(G_k + C_{3\varepsilon}G_b) - C_{2\varepsilon}\frac{\rho\varepsilon^2}{k} - R_\varepsilon + S_\varepsilon \tag{9}$$

$$C_{1\varepsilon} = 1.42; C_{2\varepsilon} = 1.68 \eta = (2E_{ij}\cdot E_{ij})^{\frac{1}{2}}\frac{k}{\varepsilon}; E_{ij} = \frac{1}{2}\left(\frac{\partial v_i}{\partial x_j} + \frac{\partial v_j}{\partial x_i}\right) \tag{10}$$

Where k is the turbulent kinetic energy, m^2/s^2; v is the velocity of the fluid, m/s. I is unit tensor. ε is the Dissipation of k, m^2/s^3; The terms that generate kinetic energy in turbulence as a result of average velocity gradients and buoyancy are G_k and G_b. The dissipation rate resulting from the variable dilatation in compressible turbulence is represented by Y_M (Gu et al., 2021). α_k and α_ε are the turbulent Prandtl numbers in k and ε equations, which are equal to 1.39. $C_{1\varepsilon}$, $C_{2\varepsilon}$ are the dimensionless empirical constant.

3. Results

3.1. Corrosion rate variation of N80 steel under different flow regimes

The variation of v_{corr} on N80 steel exposed to high-mineralization oilfield-produced water at different flow velocities are shown in Fig. 3. The v_{corr} values under the laminar flow regime at both temperatures were lower than the corresponding values under stationary and turbulent flow regimes. At 80 °C, v_{corr} initially increases significantly with increasing v_{rs}, before gradually stabilizing to a value of approximately 14.83 mm/a upon reaching the v_{rs} of 500–660 rpm. At 150 °C, however, v_{corr} reaches a maximum value of 8.15 mm/a at 300 rpm, before gradually decreasing with further increase in v_{rs}, reaching 3.01 mm/a at 660 rpm. Overall, the v_{corr} values at 150 °C are considerably lower than those at 80 °C, which is likely attributed to the different protective properties of the corrosion scale at these two temperatures.

3.2. Characterization of corrosion morphology and composition at 80 °C

The morphology and composition of corrosion scales on N80 steel at 80 °C are shown in Figs. 4 and 5, respectively. At 0 rpm, the

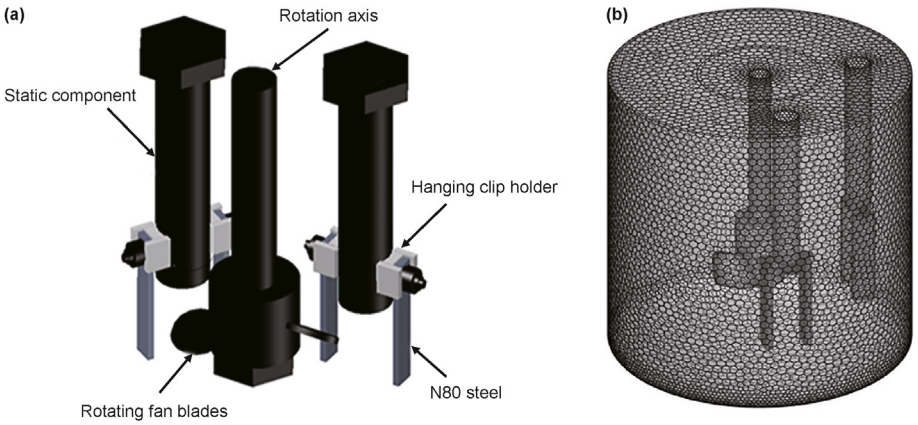

Fig. 2. **(a)** Rotating reactor model; **(b)** Schematic of reactor mesh sectioning.

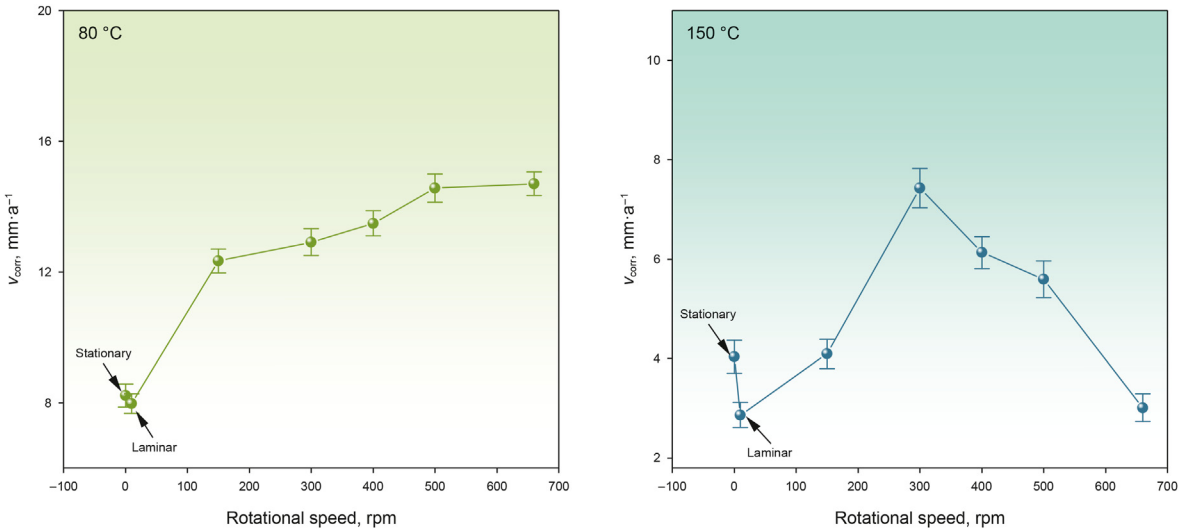

Fig. 3. Variation of v_{corr} on N80 steel with rotational speed at 80 and 150 °C.

corrosion scale is relatively loose and porous, and the high magnification image reveals a conspicuous white grid-like amorphous structure. XRD spectroscopy analysis revealed that no typical crystal features or carbonates were detected, and only the Fe peak was present. However, as the v_{rs} was increased, dendritic crystal structures were observed on the corrosion scale. In particular, the dendritic crystal density on the surface layer was highest at 10 rpm. As the v_{rs} was increased to the turbulent flow regime (300 rpm and 660 rpm were selected for characterization), the coverage of the dendritic crystals in the surface layer decreased, and the crystals became finer.

The XRD results in Fig. 5 show that the dendritic structures observed under flow regimes mainly consisted of aragonite calcium carbonate ($CaCO_3$) crystals. This is consistent with previous studies by Jones et al. (Jones and Peng, 2014; Jones, 2017) and Ren et al. (2021). A comparison of the XRD spectra at 300 and 660 rpm reveals that low-intensity cementite (Fe_3C) peaks at a diffraction angle of 37.8° were present, with low-intensity Fe_3C peaks at 45° also appearing at 660 rpm, indicating that increasing the v_{rs} favors Fe_3C formation. Additionally, the dendritic structure of aragonite $CaCO_3$ crystals does not provide corrosion protection in combination with the v_{corr} variation at 80 °C. As the v_{rs} increases (under the turbulent flow regime), the coverage of the corrosion scales and the crystal size of aragonite $CaCO_3$ are both reduced. The dendritic aragonite $CaCO_3$ structures promote corrosion by increasing the specific surface area of corrosive ion adsorption carriers (Alwis et al., 2021; Ren et al., 2021).

To further validate the composition of the dendritic crystals, EDS spot scanning was used to confirm the specific elemental compositions at different locations in the corrosion scale, with the results displayed in Fig. 6 and Table 4. It is evident that no elemental Ca is detected at both scanned positions at 0 rpm, and Fe and C were the first and second most abundant elements, respectively, in the white corrosion scale at position 1. This indicates that the white flocculent structure of the corrosion scale layer at 0 rpm likely consists of Fe_3C, while position 2 contains the N80 steel substrate. Thus, there is no $CaCO_3$ formation at 0 rpm despite the high Ca^{2+} concentration in the solution. Under the laminar and turbulent flow regimes, however, the EDS point scanning of the dendritic crystals formed revealed a significant amount of Ca, further indicating through the

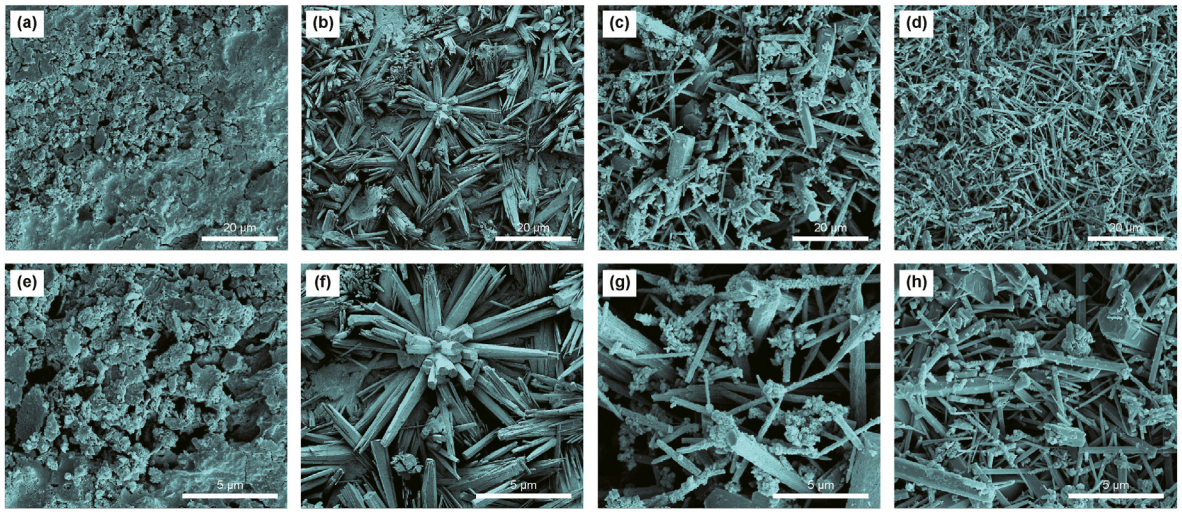

Fig. 4. SEM images of corrosion morphology formed on the surface of N80 steel at 80 °C. **(a)** 0 rpm, **(b)** 10 rpm, **(c)** 300 rpm, **(d)** 660 rpm; High magnification: **(e)** 0 rpm, **(f)** 10 rpm, **(g)** 300 rpm, **(h)** 660 rpm.

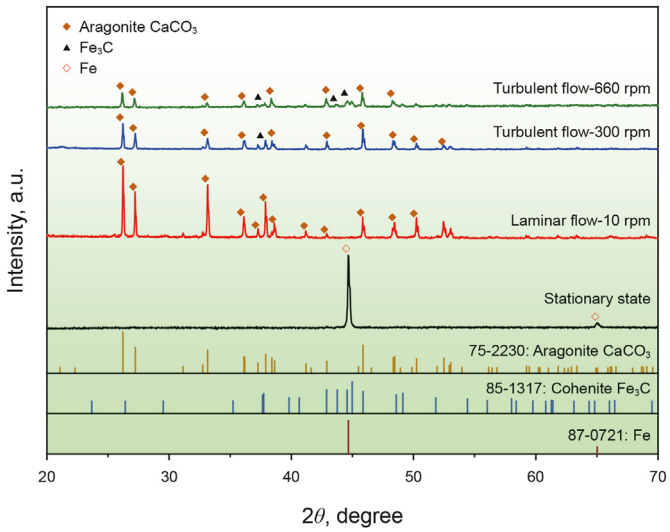

Fig. 5. XRD spectrum of corrosion scales in different flow regimes at 80 °C.

atomic content ratio that the main component of the dendritic structure was $CaCO_3$. Moreover, the presence of protective $FeCO_3$ crystals was not detected, suggesting that $FeCO_3$ deposition was inhibited by the high Ca^{2+} concentration (Shamsa et al., 2019). As the v_{rs} increased to the turbulent flow regime, an accumulation of white agglomerated floccules appeared around the dendritic aragonite $CaCO_3$ crystals. The EDS results indicate that the corrosion scales consisting of white agglomerated floccules is Fe_3C, the

Table 4
Statistics of elemental content of corrosion scales at 80 °C (at.%).

Position	C	O	Fe	Ca
0 rpm-1	38.05	3.29	58.66	0.00
0 rpm-2	7.64	0.00	92.36	0.00
10 rpm-1	20.59	31.12	0.00	48.29
10 rpm-2	8.18	56.34	20.76	14.72
300 rpm-1	11.95	24.29	61.33	2.43
300 rpm-2	29.30	35.30	0.93	34.47
660 rpm-1	14.50	16.28	68.06	1.16
660 rpm-2	9.60	49.08	3.79	37.53

existence of which is attributed to potential differences of corrosion in the metallographic microstructure of the steel. Ferrite in the N80 steel matrix is preferentially dissolved due to its higher electronegativity, while Fe_3C acts as a cathode on the surface of the substrate (Lu, 2008; Akeer, 2014; Wei et al., 2018). Specifically, Fe_3C produced by the dissolution of N80 steel attaches to the substrate surface and acts as an interfacial conductor to form α-Fe microcells, which promotes electrochemical corrosion (Neville et al., 2015; Ochoa et al., 2015; Zhang et al., 2021). As such, the presence of Fe_3C is not purely detrimental, as it can serve as a point of attachment for carbonate precipitates, such as $FeCO_3$ and $CaCO_3$, thereby promoting the nucleation growth of carbonate crystals (Al-Hassan et al., 1998).

3.3. Characterization of corrosion morphology and composition at 150 °C

The differences in corrosion scale morphology exhibited by N80 steel at 150 °C are shown in Fig. 7. At 0 rpm, the corrosion scales on

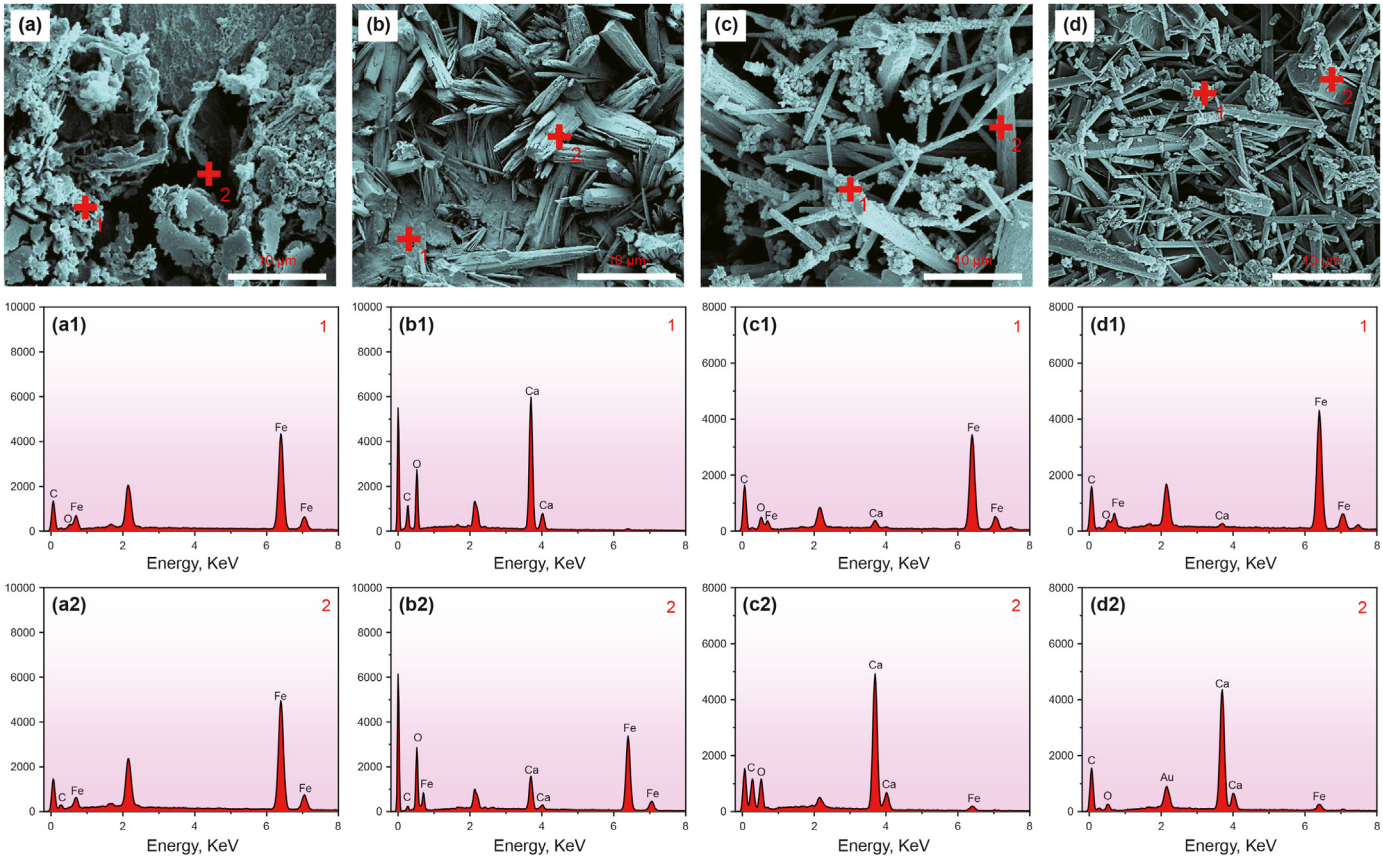

Fig. 6. EDS spot scanning of corrosion scales under different v_{rs} at 80 °C (at.%). **(a)** 0 rpm, **(b)** 10 rpm, **(c)** 300 rpm, **(d)** 660 rpm.

the substrate surface were characterized by the coexistence of dendritic crystals and cubic massive crystals. At high magnification, the corrosion morphology at 0 rpm exhibits a multi-layered phenomenon, and there is a clear porosity between the corrosion scale of different structures. In the laminar flow regime (10 rpm), the corrosion morphology becomes increasingly dense and shows the interaction of dendritic crystals and massive crystals. The dense corrosion scale layer effectively prevents the corrosive medium from penetrating, resulting in a decreased v_{corr}. When the v_{rs} is further increased to the turbulent flow regime, the corrosion scales present a blocky polygonal crystal structure. Moreover, the size of the bulk crystal structure expands with the increase in v_{rs}, which indicates the promotion of superficial polygonal bulk crystals. Nevertheless, the growth of large-size massive crystal stacks also results in the emergence of large voids between the crystals. At 660 rpm, the appearance of crystal stacking voids also induces the accumulation of white corrosion scale.

The XRD results of scale formation and EDS results of different regions of corrosion scale for N80 steel in different flow regimes are presented in Figs. 8 and 9, respectively. XRD spectra show that the corrosion scale composition of the substrate surface at 0 rpm and 10 rpm is $FeCO_3$ and a small amount of aragonite $CaCO_3$. Combined with the EDS spot-scan results (Fig. 9 and Table 5), the massive crystals at 0 rpm are $FeCO_3$ and the dendritic structure is aragonite $CaCO_3$. The lattice structure of the petal-like stacks in the surface layer at 10 rpm is mainly composed of Fe_3C and $FeCO_3$. As the v_{rs} is further increased to the turbulent flow regime, the main components of the corrosion scale are calcite $CaCO_3$ and $FeCO_3$. The EDS spot-scan results also further confirmed that the massive multilateral crystals formed in the turbulent flow regime were $CaCO_3$, and the white corrosion scale embedded between the voids of the multilateral crystals was $FeCO_3$. Consequently, the increase in v_{rs} at 150 °C facilitates the conversion of aragonite $CaCO_3$ to calcite $CaCO_3$. On the other hand, it also promotes the growth of calcite $CaCO_3$ crystals.

3.4. Effect of fluid flow on the cross-sectional morphology

The cross-sectional morphology and EDS line sweeps of the corrosion scale under the different flow regimes at 80 °C are shown in Fig. 10. The corrosion scale at 0 rpm is thin and loose (8.4 μm),

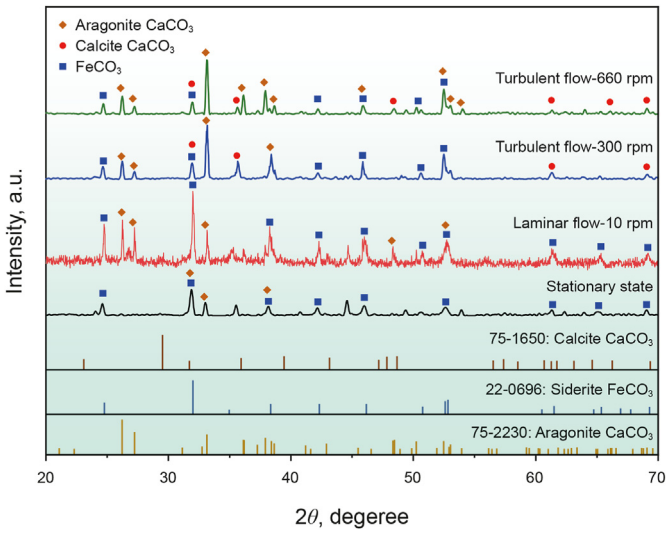

Fig. 8. XRD spectrum of corrosion scales in different flow regimes at 150 °C.

with a large crack between the film layer and the substrate, suggesting poor adhesion between the two. Under the laminar flow regime (10 rpm), however, the corrosion scale shows obvious stratification and its loosely accumulated. The EDS line scanning results reveal that the surface scale is mainly composed of Fe and C at 0 rpm, thus predominantly composed of Fe_3C. At 10 rpm, Ca content dominates the entire corrosion layer, and a lattice-like layer of Fe_3C is scattered over the Ca-rich inner layer of the corrosion scale.

Under the turbulent flow regime, the cross-sectional morphology exhibits a lattice-like skeleton structure, with an outer layer consisting of dendritic aragonite-type $CaCO_3$ and an inner layer consisting of mainly lattice-like Fe_3C. The thicknesses of both layers decreased as v_{rs} increased from 300 to 660 rpm. Specifically, the outer $CaCO_3$ layer decreased from 37 to 15.6 μm, while the inner Fe_3C layer decreased from 61 to 48.7 μm. Increasing the v_{rs} produces a denser and finer dendritic aragonite $CaCO_3$, which also significantly enhances the densification of the inner Fe_3C. Whereas, the v_{corr} did not decrease with increasing film thickness

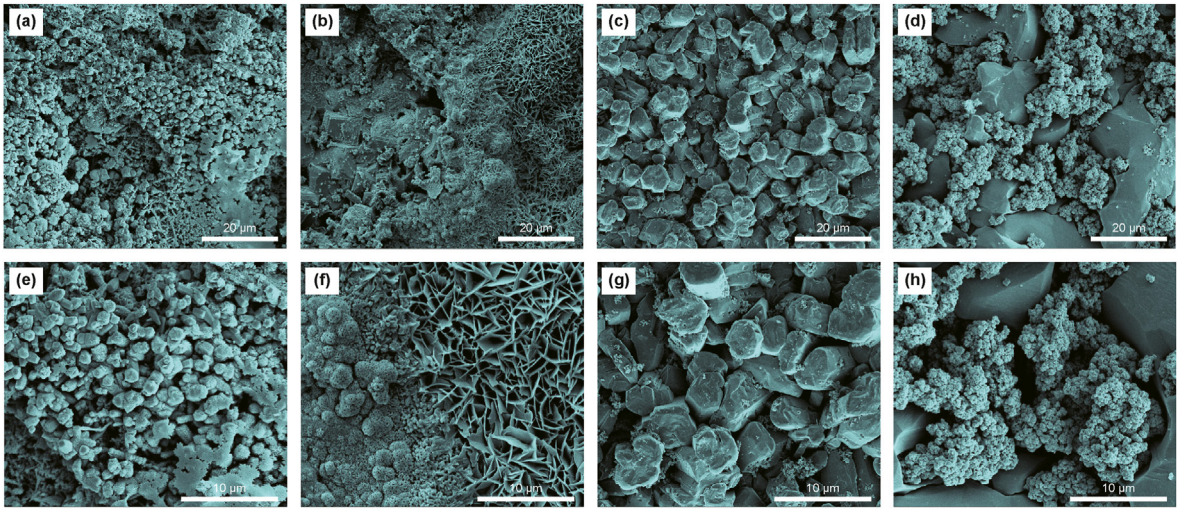

Fig. 7. SEM image of corrosion morphology formed on the surface of N80 steel at 150°. **(a)** 0 rpm, **(b)** 10 rpm, **(c)** 300 rpm, **(d)** 660 rpm; High magnification: **(e)** 0 rpm, **(f)** 10 rpm, **(g)** 300 rpm, **(h)** 660 rpm.

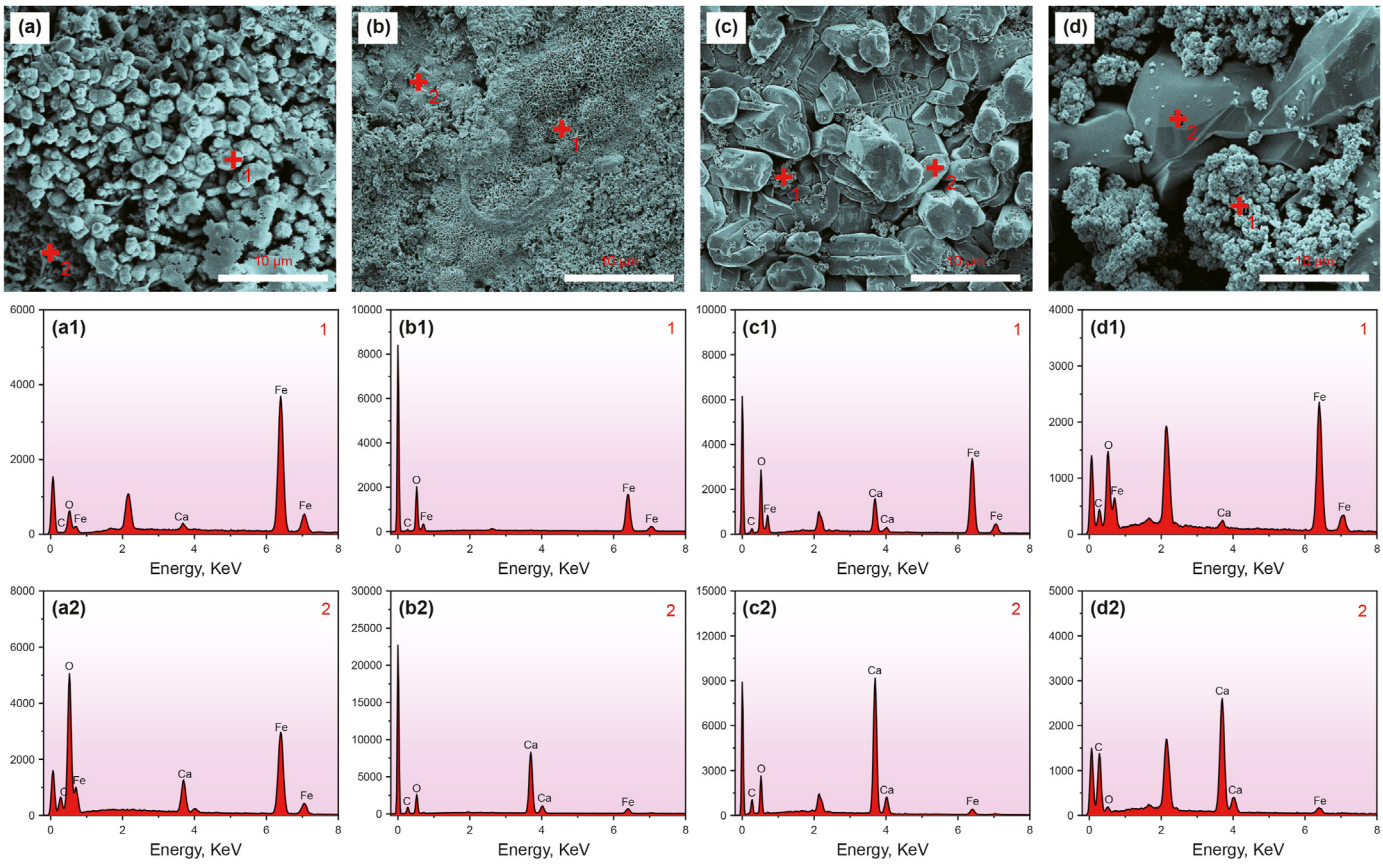

Fig. 9. EDS spot scanning of corrosion scales under different v_{rs} at 150 °C (at.%). **(a)** 0 rpm, **(b)** 10 rpm, **(c)** 300 rpm, **(d)** 660 rpm.

Table 5
Statistics of elemental content of corrosion scales at 150 °C (at.%).

Position	C	O	Fe	Ca
0 rpm-1	0.87	27.36	70.13	1.64
0 rpm-2	15.79	58.39	9.14	16.68
10 rpm-1	7.70	62.74	28.53	1.03
10 rpm-2	16.91	62.80	2.88	17.40
300 rpm-1	12.33	58.17	26.77	2.73
300 rpm-2	17.28	63.02	1.47	18.23
660 rpm-1	28.61	47.29	23.40	0.70
660 rpm-2	62.02	21.51	1.45	15.02

under turbulent conditions. This further suggests that the enhanced densification of the corrosion scale layer at 80 °C does not hinder the corrosion process. The combination of dendritic aragonite-type $CaCO_3$ and Fe_3C does not provide corrosion protection.

The cross-sectional morphology and EDS line sweeps of the corrosion scales under the different flow regimes at 150 °C are shown in Fig. 11. The corrosion scale at 150 °C presents a multilayer structure and the densification is far superior to that of 80 °C. Specifically, at 0 rpm, the outer layer of the corrosion scale is predominantly composed of $CaCO_3$ and a small amount of $FeCO_3$, with a thickness of 2.8 μm; the middle layer is $CaCO_3$, with a thickness of 5.6 μm; and the inner layer is mainly $FeCO_3$, with a thickness of 11.4 μm. Under the laminar flow regime (10 rpm), the interactive growth of $CaCO_3$ and $FeCO_3$ was observed. Among them, $CaCO_3$ was mainly distributed in the middle of the corrosion scale layer, with a thickness of 10.13 μm; while $FeCO_3$ was scattered throughout the whole corrosion scale layer, with a total thickness of about 21.27 μm.

Another effect observed under turbulence was the presence of a pronounced "sandwich" structure in the cross-sectional morphology. At 300 rpm, the outer, middle, and inner layers consisted of $FeCO_3$ (outer layer thickness 16.25 μm), $CaCO_3$ with some porosity defects (middle layer thickness 24.45 μm), and $FeCO_3$ with poor densification and homogeneity (inner layer thickness 9.59 μm), respectively. As the v_{rs} increases to 660 rpm, the outer layer consists of $FeCO_3$ with a thickness of 11.6 μm. This provides further evidence that the white corrosion scale situated in the upper part of the massive multilateral calcite is mainly composed of $FeCO_3$. Further, the dense middle layer consists of $CaCO_3$ with a thickness of 28.4 μm, while the more uniformly distributed inner layer consists of $FeCO_3$ with a thickness of only 7.0 μm. Consequently, increasing v_{rs} at 150 °C dramatically promoted the growth of calcite-type $CaCO_3$.

3.5. Effect of fluid flow on localized corrosion behavior

The pitting microscopic contours of the N80 steel samples were determined to clarify the local corrosion behavior under different flow regimes, as shown in Figs. 12 and 13. Since no pits were found in the laminar regime at either temperature, it is not discussed here.

At 80 °C, both the depth and coverage of pitting noticeably expanded as the v_{rs} increased from stationary to turbulent flow regime (300 rpm), while the shape of the pitting defects changed from small hole-shaped to disc-shaped. As the v_{rs} was further increased to 660 rpm, no pitting defects were observed on the profile surface after corrosion scale removal. This may be accounted

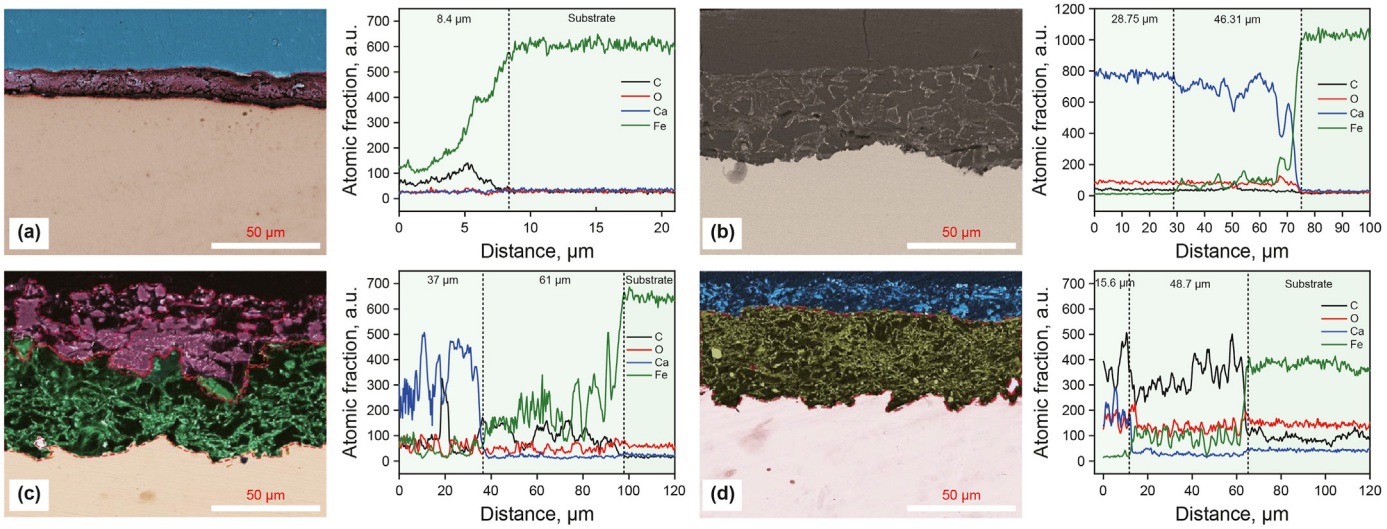

Fig. 10. Cross-sectional morphology and EDS line scanning of corrosion scales in different flow regimes at 80 °C, **(a)** 0 rpm, **(b)** 10 rpm, **(c)** 300 rpm, **(d)** 660 rpm.

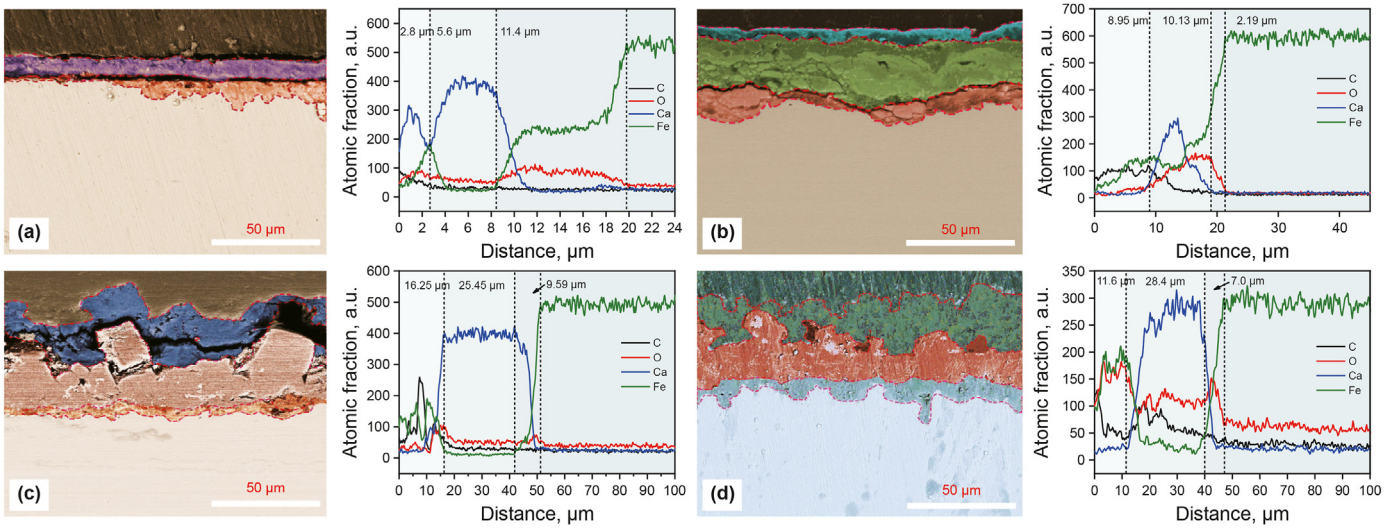

Fig. 11. Cross-sectional morphology and EDS line scanning of corrosion scales in different flow regimes at 150 °C, **(a)** 0 rpm, **(b)** 10 rpm, **(c)** 300 rpm, **(d)** 660 rpm.

by the higher v_{corr} at 660 rpm, which partially obscures the actual pitting development kinetics, which results in the substrate around the pits being dissolved at a relatively high rate (Shamsa et al., 2019).

At 150 °C, a similar trend was observed with increasing v_{rs} up to 300 rpm, with the depth and coverage of pitting defects increasing even faster than at 80 °C. As the v_{rs} was further increased to 660 rpm, the pitting defects became interconnected and their surface coverage was further enlarged. These results indicate that the elevated in temperature facilitates an increase in the number of corrosion pits and the pitting depth, while increasing the v_{rs} facilitates the expansion of the pitting area. Thus, it is reasonable to assume that both high temperatures and relatively high v_{rs} are needed to induce pitting initiation and propagation. This further validates the findings of Elgaddafi et al. (2021) obtained under high temperature and high-speed Couette flow regimes.

In addition, Gumbel probability distributions were plotted by performing 16 repetitions of pitting depth tests on N80 steel specimens at different v_{rs}. The Gumbel probability plots in Fig. S1 show that the pitting depth data at 80 and 150 °C are consistent with the Gumbel distribution. The scale parameter (σ) and positional parameter (λ) of the pitting depths of N80 steel estimated using the Gumbel distribution function for different v_{rs} impacts are listed in Table S1. The Gumbel probability plot at 80 °C shows two distinct linear segments, while only one linear segment exists at 150 °C. This suggests that pitting pits at 150 °C are more likely to develop into perforations. Moreover, the increase in rotational speeds at 80 °C contributes to the increase in the pitting depth, while the effect of rotational speeds is weaker at 150 °C and shows a stable pit development at 300 rpm.

4. Discussion

4.1. Analysis of corrosion scale evolution mechanism

4.1.1. Effect of temperature on the characteristics of corrosion scales

The precipitation of $CaCO_3$ and $FeCO_3$ crystals on the substrate surface involves interaction between supersaturation, nucleation, and crystal growth processes (Esmaeely et al., 2013). Supersaturation (S), which is commonly used to measure the sedimentary

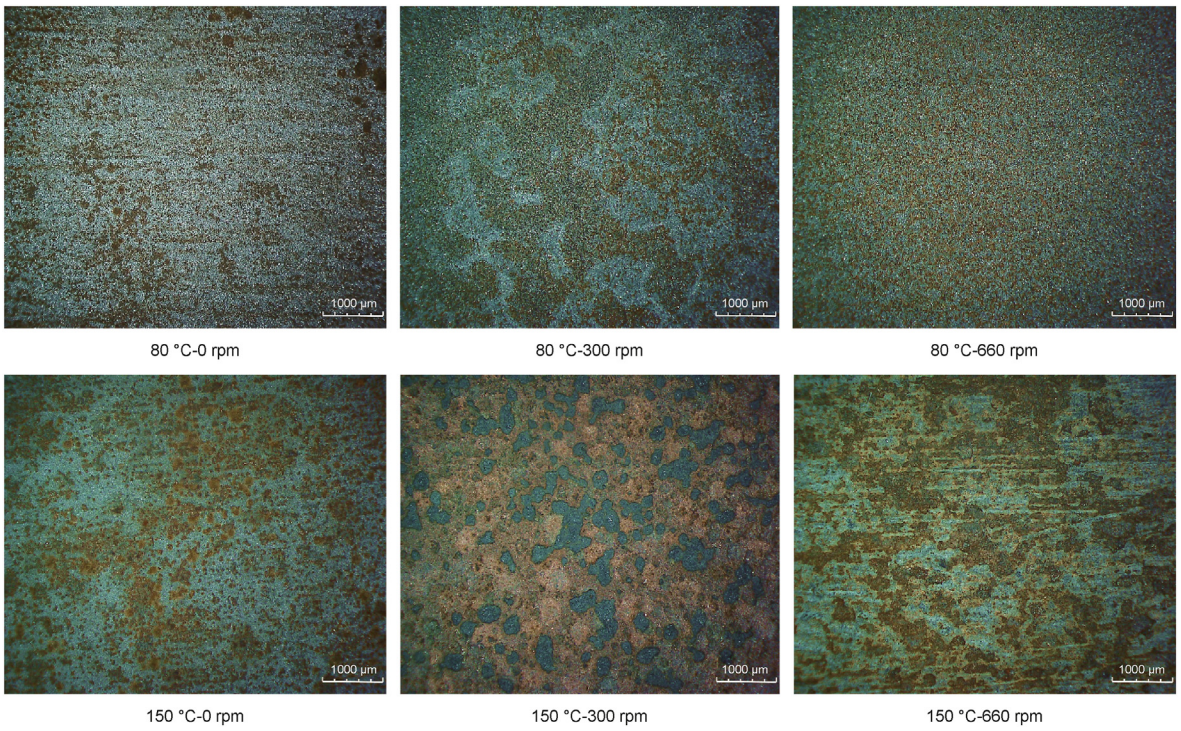

Fig. 12. 2D morphological characterization of N80 steel after corrosion scales removal.

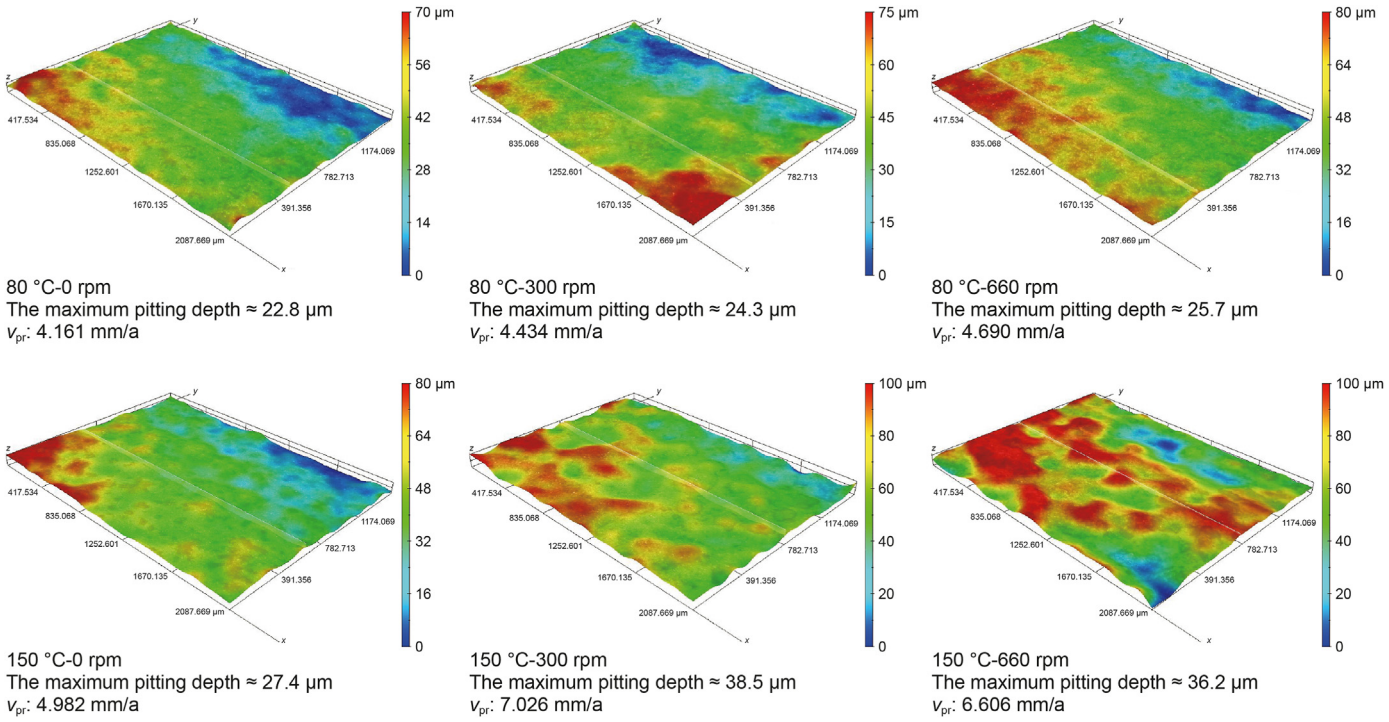

Fig. 13. 3D morphological characterization of N80 steel after corrosion scales removal.

dynamics of carbonate crystals (Guo et al., 2012; Wang et al., 2022b), is the ratio of the concentration product of the anions and cations comprising the carbonate crystals to the solubility product (K_{sp}). The value of S relates to the kinetics of carbonate crystal deposition. When $S < 1$, the solution is unsaturated, and no nucleation (and therefore growth) of carbonate crystals occurs. When $S > 1$, the concentration of ions forming the carbonate crystals exceeds the K_{sp} of the crystals. Carbonate crystals can be significantly deposited only when the nucleation rate exceeds the critical supersaturation (S_c) (Drela et al., 1998; Wang et al., 2022b). Moreover, S increases exponentially with crystal nucleation and linearly with crystal growth (Yin et al., 2009; Gao et al., 2011). Thus,

crystal growth dominates when S is comparatively low, resulting in the formation of large, dispersed crystals (Shamsa et al., 2019; Wang et al., 2022b). In contrast, crystal nucleation dominates if S is sufficiently high, forming the smaller-sized crystals or even amorphous layers (Nešsić, 2006; Gao et al., 2011). The supersaturation calculations for $FeCO_3$ and $CaCO_3$ were performed according to Eqs. (11) and (12), respectively:

$$S_{FeCO_3} = \frac{c_{Fe^{2+}} \cdot c_{CO_3^{2-}}}{K_{sp,FeCO_3}} \tag{11}$$

$$S_{CaCO_3} = \frac{c_{Ca^{2+}} \cdot c_{CO_3^{2-}}}{K_{sp,CaCO_3}} \tag{12}$$

Where, $c_{Fe^{2+}}$, $c_{Ca^{2+}}$ and $c_{CO_3^{2-}}$ are the concentrations of Fe^{2+}, Ca^{2+} and CO_3^{2-} in the simulated formation water system, respectively. Since $MgCO_3$ was not detected in the corroded scales, the thermodynamic deposition process of $MgCO_3$ was not taken into consideration. $K_{sp,FeCO_3}$ and $K_{sp,CaCO_3}$ are the solubility constants of $FeCO_3$ and $CaCO_3$. Further, K_{sp} presents a well correlation with temperature. The K_{sp} of $FeCO_3$ and $CaCO_3$ have been elaborated by Bénézeth et al. (2009, 2011), Neerup et al. (2023) and Dorange et al. (2005), as shown in Eqs. (13) and (14).

$$\log K_{sp,FeCO_3} = 175.568 - \frac{6738.483}{T_K} + 0.0139T - 67.898 \log T \tag{13}$$

$$\log K_{sp,CaCO_3} = -7.8156 - \frac{1502}{T_K} + 0.0311T + 5.518 \log T \tag{14}$$

where T_K is the temperature in Kelvin. The calculated K_{sp} of carbonate crystals is shown in Table 6. At 80 °C, the K_{sp} values were in the order of $K_{sp,FeCO_3} < K_{sp,CaCO_3}$. This means that $FeCO_3$ reaches saturation before $CaCO_3$. Additionally, Ca^{2+} originates from the brines, and Fe^{2+} originates from the active dissolution of the N80 steel during the crystal nucleation process. The concentration of Ca^{2+} is much higher than Fe^{2+}. Ca^{2+} concentration is always supersaturated. The concentration product $c_{Ca^{2+}} \cdot c_{CO_3^{2-}}$ plays a more significant role in the crystal supersaturation deposition kinetics, which leads to the precipitation of $CaCO_3$ in preference to $FeCO_3$. Further, Alsaiari et al. (2009) found that higher concentrations of Ca^{2+} inhibited the nucleation and growth of $FeCO_3$ through altering the solubility of $FeCO_3$. The preferential deposition of $CaCO_3$ also occupies the CO_3^{2-} and HCO_3^-, resulting in S_{FeCO_3} being <1 at 80 °C, which hinders the deposition of $FeCO_3$ crystals (Shamsa et al., 2019; Rizzo et al., 2020). Thus, the corrosion scale at 80 °C was mainly composed of $CaCO_3$, and the absence of $FeCO_3$ was confirmed by the XRD EDS line scanning results.

Interestingly, the XRD and EDS line scanning results at 150 °C under different flow regimes revealed a "sandwich" structure of the surface corrosion scale, with $FeCO_3$ in the inner and outer layers and $CaCO_3$ in the middle layer. This can be attributed to the K_{sp}, $FeCO_3$ is much smaller at 150 °C than at 80 °C. The increase in temperature facilitates the nucleation and growth of $FeCO_3$ crystals.

Table 6
K_{sp} values of carbonate crystals at 80 and 150 °C.

T, °C	$FeCO_3$	$CaCO_3$
80	2.48×10^{-12}	1.01×10^{-9}
150	1.55×10^{-13}	9.20×10^{-11}

On the other hand, the active dissolution of the N80 steel is more likely to occur over a shorter period at high temperatures, as demonstrated by Shamsa et al. (2019) in 150 °C aqueous solutions containing NaCl and $CaCl_2$. By contrast, the concentration of Fe^{2+} at 150 °C is more abundant than at 80 °C, which in turn facilitates $FeCO_3$ deposition. Therefore, Ca^{2+} did not effectively inhibit the nucleation of $FeCO_3$ as it did at 80 °C. Moreover, $CaCO_3$ crystals show pronounced growth with increasing v_{rs} instead of being controlled by crystal nucleation. This can be attributed to a lower S_{CaCO_3} at 150 °C and competitive deposition adsorption between Fe^{2+} and Ca^{2+} occurs at higher v_{rs}. The $FeCO_3$ crystals of the inner layers provide active sites for the growth of $CaCO_3$ crystals (Alsaiari et al., 2009). The $CaCO_3$ also transitions from aragonite to the more stable calcite form with increasing v_{rs}. Besides, v_{corr} at 150 °C is much lower than 80 °C according to Fig. 3, indicating that the deposition of calcite $CaCO_3$ + $FeCO_3$ provides more effective protection than aragonite $CaCO_3$ + Fe_3C.

4.1.2. Effect of flow regime on the thickness variation of corrosion scale

At 80 and 150 °C, the thickness of the corrosion scale layer increases with v_{rs} during the transition from static to turbulent flow. This can be ascribed to the combination of mass transfer and thermodynamics, which significantly promotes the dissolution of the substrate. As a result, ferrite is preferentially dissolved in the N80 steel substrate, allowing large amounts of skeleton-like Fe_3C and Fe^{2+} to co-aggregate on the substrate surface. Flow mass transfer also enhances the contact frequency between Ca^{2+}, Fe^{2+} and HCO_3^-, which contributes to the nucleation and growth of carbonate crystals (Paolinelli and Carr, 2015). Moreover, the skeleton-like Fe_3C also provided a target for the deposition of carbonate crystals, which in turn led to the gradual thickening of the corrosion scale layer.

The cross-sectional morphologies in Figs. 10 and 11 show that the thicknesses of the aragonite $CaCO_3$ + Fe_3C (at 80 °C) and $FeCO_3$ (at 150 °C) corrosion scale layers decreased with increasing the v_{rs} under turbulent regimes. As we know, corrosion scale is subject to wall shear stress (τ_w) and erosion by weakly acidic solutions (Paolinelli and Carr, 2015). The increase of v_{rs} can strengthen the turbulent kinetic energy and τ_w, as demonstrated by Tan et al. (2020) and Yang et al. (2010, 2022). The strengths of the loose and dense corrosion scales were in the range of 137.2–148.3 Pa and 1–10 MPa (Tan et al., 2020). The τ_w on the corrosion scale can be ascertained from the tribological damage along the circumferential line of the surface, as follows:

$$\tau_w = \left(\frac{f}{2}\right)\rho v(\pi DN)^2 \tag{15}$$

Where v is the fluid line velocity, m/s; f is the Fanning friction coefficient. The Fanning coefficient of friction can be simplified by using the Theodorsen-Regier law of empirical friction of rotating cylinders in turbulent regimes by Theodorsen et al. (1944):

$$\frac{f}{2} = 0.0791Re^{-0.3} \tag{16}$$

The maximum value of τ_w calculated based on Eq. (15) for different flow rates is 8.76 Pa, as shown in Table 7, which is much smaller than the minimal value required for the breakdown of the $FeCO_3$ layer as suggested by Tan et al. (2020). Consequently, τ_w does not cause mechanical stripping of the corrosion scale, which is also in agreement with the results of Wang et al. (2022b) and Ruzic et al. (2006).

So, what exactly causes the corrosion scale thickness to

decrease? Consider that the pH of oilfield-produced water usually varies between 4 and 6, which is only weakly acidic. However, as a lower pH range than this is more favorable towards the dissolution of carbonate crystals (Nešsić, 2006), Nešsić et al. (2006) found that the dissolution of the corrosion scale is dominated by mass transfer processes. Thus, the dissolution kinetics are highly dependent on the brine saturation as well as the v_{rs} (Ruzic et al., 2007). The flow dependence of corrosion scale dissolution is positively correlated with temperature and negatively with pH (Nešsić, 2006; Ruzic et al., 2007).

In light of the aforementioned analysis, the pH of the corrosive brines was determined (Fig. 14). The pH drops with increasing the v_{rs} at both temperatures, as the formation of internal vortices within the reactor (Ye et al., 2022). This facilitates sufficient mixing between upper-phase CO_2 and highly-mineralized formation water, thereby enhancing the solution acidity (Masuda et al., 2019; Ye et al., 2022). In addition, the inner Fe_3C grid structure becomes denser with increasing v_{rs}. This is because Fe_3C establishes galvanic corrosion pairs with the substrate due to its electrochemical properties, with Fe_3C acting as the cathode and the bare steel substrate acts as the anode (Owen et al., 2022). A significant increase in v_{pr} is observed in Fig. 13. Simultaneously, the Fe_3C attached to the surface of dendritic aragonite $CaCO_3$ crystals triggers localized acidification due to galvanic interaction (as shown in Eqs. (17) and (18)), leading to the degradation of the outer $CaCO_3$ (Crolet et al., 1996; Owen et al., 2022).

$$CO_{2(g)} + H_2O_{(l)} \rightarrow H_2CO_{3(l)} \tag{17}$$

$$H_2CO_3 \rightarrow H^+ + HCO_3^- \tag{18}$$

$$HCO_3^- \rightarrow H^+ + CO_3^{2-} \tag{19}$$

Further, the pH value at 150 °C is higher than 80 °C. This can be explained by Henry's law, as shown in Eq. (20). At higher temperatures, the volatility of the solute CO_2 induces to an increase in Henry's coefficient and therefore a reduced solubility.

$$P_g = K_H \times C \tag{20}$$

$$Ca^{2+} + HCO_3^- \rightarrow CaCO_3 + H^+ \tag{21}$$

where P_g is the partial pressure of CO_2 in aqueous solution; K_H is Henry constant; C is the fraction of CO_2 in aqueous solution. Additionally, the growth of $CaCO_3$ crystals induces localized acidification in the steel substrate, as reflected in Eq. (21). Both of these pH-lowering mechanisms result in the dissolution of the $FeCO_3$ protective layer; consequently, the thicknesses of both the innermost and outermost $FeCO_3$ layers decreased with increasing the v_{rs}, as shown in Fig. 10. Nevertheless, the higher density of the inner $FeCO_3$ layer at 150 °C and 660 rpm compared with that at 150 °C and 300 rpm provides a more effective barrier to corrosion.

Table 7
Fluid parameters at different temperatures and Reynolds number changes at different speeds.

T, °C	v_{rs}, rpm	τ, Pa
80	0	–
	10	0.01
	150	0.72
	300	2.33
	400	3.78
	500	5.5
	660	8.76
150	0	–
	10	0.01
	150	0.54
	300	1.76
	400	2.85
	500	4.15
	660	6.62

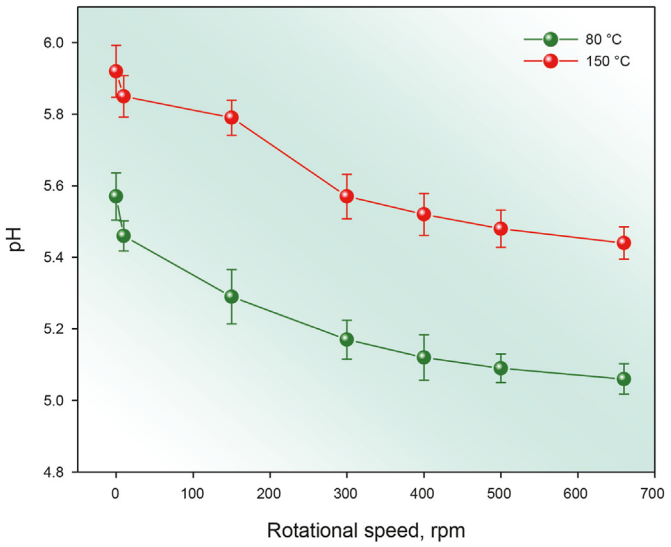

Fig. 14. pH change of formation water after impact corrosion at different flow velocities.

4.2. Analysis of interfacial mass transfer at different temperatures

The interfacial mass transfer of corrosive ions in the flow regime involves three processes: a convection process driven by turbulent kinetic energy, a diffusion process under the gradient of ion concentration, and the electric migration of charged ions. The equilibrium dynamics of charged ion i are described by the Nernst-Planck equation, which is adopted to depict the material flux balance of ion i (Kontturi et al., 2008):

$$\frac{\partial c_i}{\partial t} = \nabla(D_i + D_{i,T})c_i + z_i F \nabla(u_{m,j} c_i \nabla\varphi) - u \cdot \nabla c_i \tag{22}$$

Diffusion, electric migration, and convection effects are characterized by the first, second, and third terms on the right-hand side of Eq. (25), respectively. Under the turbulent flow regime, the rapid penetration of charges through the substrate-electrolyte bilayer interface can help the system maintain electrical neutrality (Paolinelli and Nesic, 2021). In this case, electromigration effects can be disregarded. The above equation can be simplified to:

$$\frac{\partial c_i}{\partial t} = \nabla(D_i + D_{i,T})c_i - u \cdot \nabla c_i \tag{23}$$

Where D_i is the diffusion coefficient, and $D_{i,T}$ is the turbulent diffusion coefficient. While D_i is intimately related to the turbulence intensity at constant solution medium. The turbulent dissipation rate, ε, is a crucial factor related to fluid mass transfer and energy conversion, as it represents the rate of conversion of turbulent kinetic energy into internal energy under the influence of molecular viscous forces.

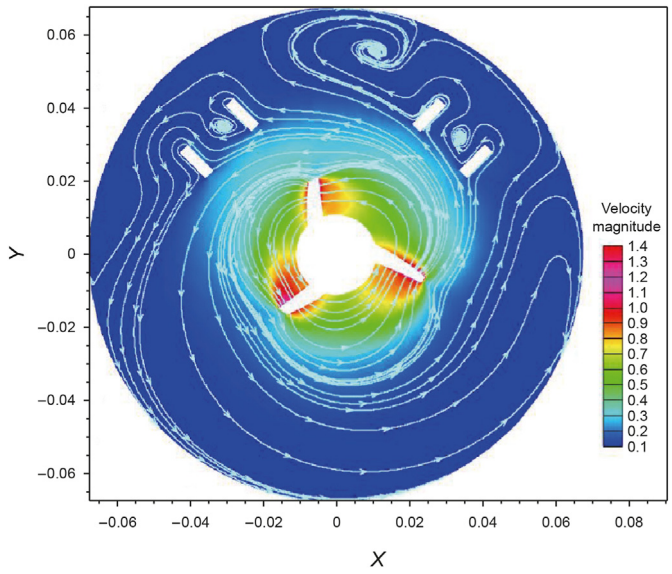

Fig. 15. Velocity vectors and vortex distribution of the flow field in the reactor.

$$\varepsilon = \frac{C_{mu}^{0.75} k^{1.5}}{l_{\mu}} \tag{24}$$

Where C_{mu} is an empirical constant, l_{μ} is the turbulent length scale.

As the v_{rs} increases in the turbulent flow regime, the higher the values of D_i and ε (Yang et al., 2022), resulting in an elevated v_{corr}. In addition, the increase in temperature enhances the heat diffusion process and the fluid vortex activity becomes more intense. Thus, there is a more pronounced rise in v_{corr} between 150 and 300 rpm at 150 °C. Specifically, the increase in v_{corr} at 150 °C is 3.1367 mm/a, while the increase at 80 °C is only 0.5788 mm/a.

Whereas, the corrosion behavior at 150 °C becomes increasingly sophisticated, as the v_{corr} no longer increases linearly with v_{rs}, instead shows a maximum value at 300 rpm before steadily declining. This may be attributed to the effects of vortices caused by large angular velocity gradients inside the reactor (Ruzic et al., 2006). The fluid undergoes rotational motion inside the vortex, with a high velocity inside the vortex and a low velocity outside, which results in momentum transfer. The evolution of the vortex core allows the flow field to be divided into several vortex cells that randomly alternate and gradually fill the entire reactor. The formation of vortex cells and full vortex structures contributes to a greater homogenization of corrosive medium such as CO_2 in the vessel and enhances the molecular mass transfer rate (Trujillo et al., 2009; Elgaddafi et al., 2021).

The velocity vectors of the flow field in the rotating reactor and the distribution of vortices around the hanging paddles are shown in Fig. 15. Fine vortices surrounding the hanging pieces and more intense vortices around the paddles. To effectively identify the vortex structures within the reactor, the classical Q criterion was employed. The distribution of vortex cell structure in the reactor is shown in Fig. 16. The vortex cells around the hanging piece are intact when v_{rs} is low. As the v_{rs} increases to 400 rpm, the vortex

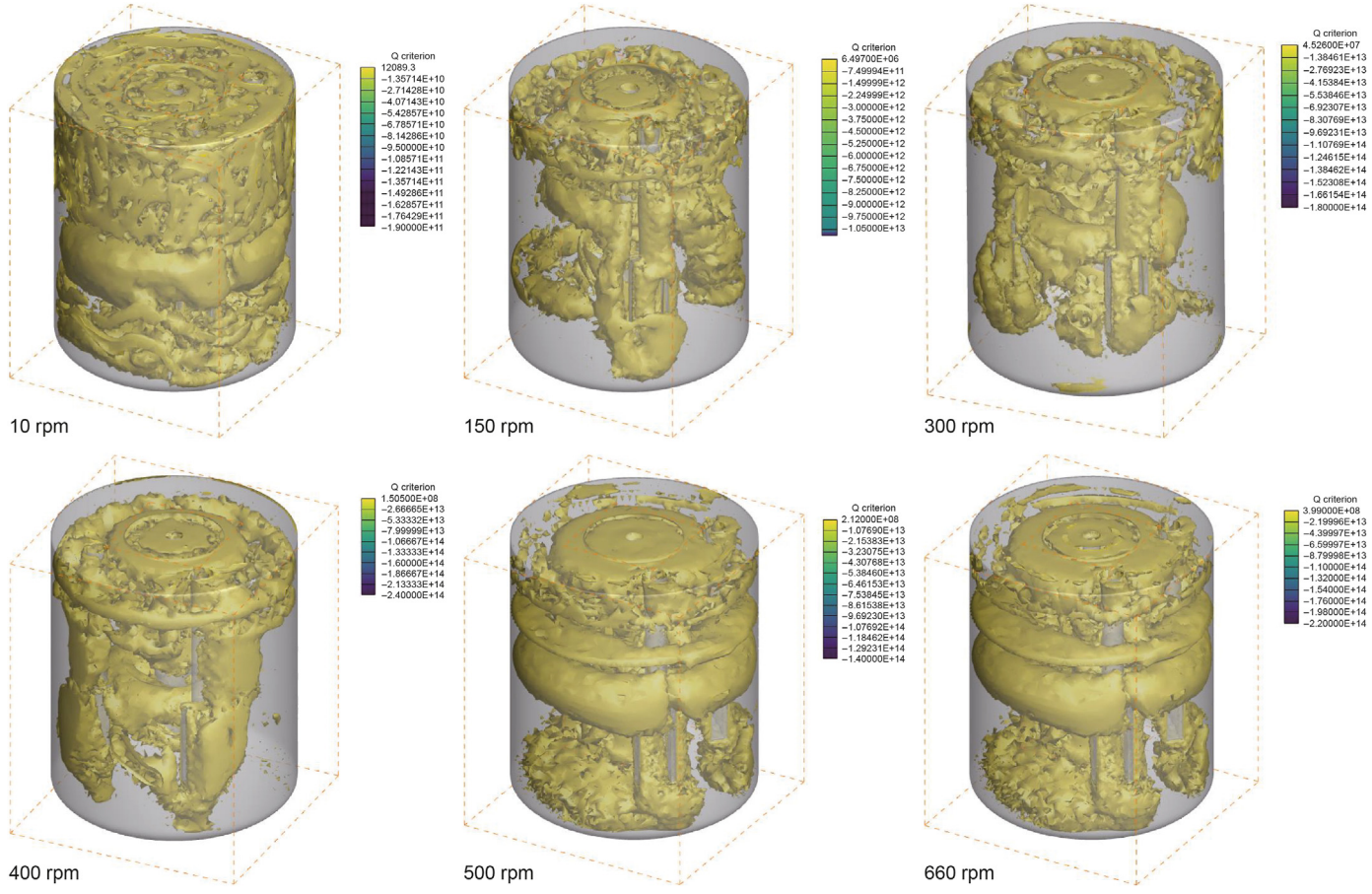

Fig. 16. Variation of vortex cell distribution inside the reactor of 150 °C.

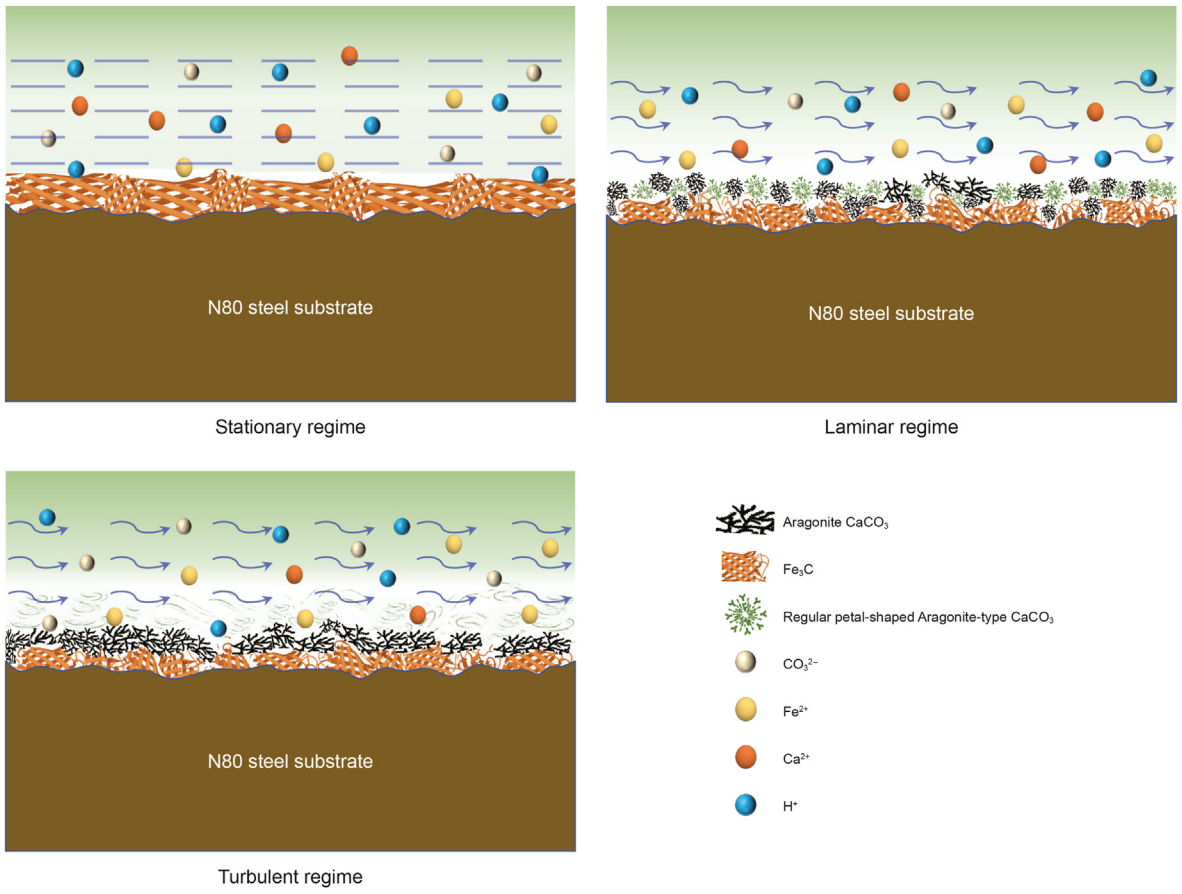

Fig. 17. Schematic corrosion mechanism of N80 steel under different flow regimes at 80 °C.

cells near the hanging piece rupture. Further increasing the v_{rs} causes the vortex cells in the lower layer of the vessel to be dissipated by the viscosity of the liquid phase molecules, and the regular vortex cell structure disappears. This implies that the *Re* value of 63669.44 at 150 °C-400 rpm has exceeded the critical rotational Reynolds number ($Re_{,c}$), as evidenced by Table 2 and Fig. 3. The disrupted vortex structure allows the flow field to begin to evolve towards undulating flow. Consequently, the molecular diffusion rate decreases significantly, and the effect of enhanced mass transfer on corrosion weakens, resulting in a maximum v_{corr} at 150 °C and 300 rpm, followed by a decrease as *Re* exceeds the critical value.

The effect of fluid viscosity on the turbulent boundary layer near the wall is also worth considering. The mass transfer of corrosive medium from the bulk solution to the electrode surface involves diffusion and convection between the turbulent layer, the buffer layer, and the viscous sublayer due to the large velocity gradient between the inner and outer sides of the boundary layer. Trujillo et al. (2009)) proposed using the Prandtl number (P_C) to characterize the variation in mass transfer resistance during turbulent processes. This equation has led to good results in mass transfer simulations.

$$P_C = A\left[\left(\frac{S_c}{S_{c,T}}\right)^{3/4} - 1\right] \tag{25}$$

where A is a constant; S_c is the Schmidt number, $S_c = \mu/\rho \cdot D$. $S_{c,T}$ is the dimensionless turbulent Schmidt number. $S_{c,T}$ can be calculated with the Kays-Crawford model (Weigand et al., 1997).

$$S_{c,T} = \left(\frac{1}{2S_{C_{T\infty}}} + \frac{0.3}{\sqrt{S_{C_{T\infty}}}}\frac{\mu_T}{\rho D_i} - \left(0.3\frac{\mu_T}{\rho D_i}\right)\left(1 - \exp\left(\frac{-\rho D_i}{0.3\mu_T\sqrt{S_{C_{T\infty}}}}\right)\right)\right) \tag{26}$$

where $S_{C_{T\infty}} = 0.85$. $S_{c,T}$ is highly dependent on distance within the boundary layer. In the buffer and turbulent layer region, corrosive species are strongly influenced by the ε, and the D_i is relatively high. According to Eqs. (25) and (26), $S_{c,T}$ is significantly elevated and P_c is subsequently reduced. Thus, below the $Re_{,c}$, the v_{corr} is promoted with the D_i. Once the $Re_{,c}$ is exceeded, the energy of the corrosive species is dissipated by the viscous. In the viscous sublayer region, the boundary layer thickness decreases and the D_i decreases as the S_c increases, indicating that the concentration gradient is localized in a narrow region close to the wall (Trujillo et al., 2009; Rivero et al., 2010). The contribution of turbulence slowly decreases closer to the wall, and the ion mass transfer from the viscous sublayer to the vicinity of the substrate is controlled by a concentration gradient (Rivero et al., 2010). Within the vicinity of the wall, the dimensionless concentration distribution C^+ was applied to evaluate the impact of mass transfer on the concentration gradient (Trujillo et al., 2009).

$$C^+ = S_{c,T}\left(\frac{1}{\kappa}\ln y^+ + 5.5 + P_c\right) \tag{27}$$

where y^+ is the distance from the substrate, κ is the von Karman

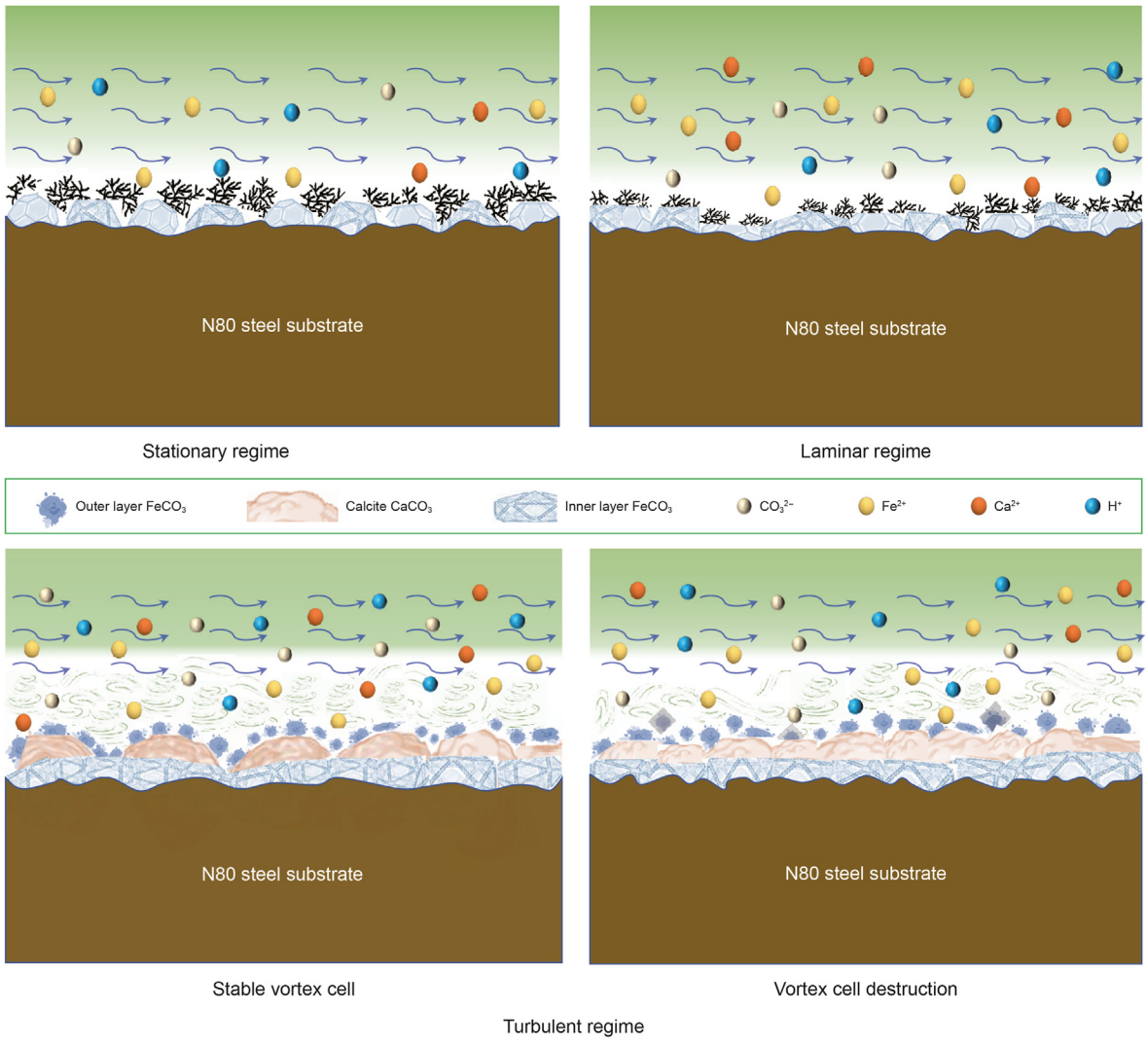

Fig. 18. Schematic corrosion mechanism of N80 steel under different flow regimes at 150 °C.

constant, and C^+ is also defined as:

$$C^+ = \frac{(C_{i,w} - C_i)C_\mu^{1/4}k^{1/2}}{J_{i,w}} \tag{28}$$

where $C_{i,w}$ represents the concentration of corrosive medium on the substrate, C_i represents the concentration at a distance $y+$ from the wall, C_μ is the constant for turbulence modeling, and $J_{i,w}$ is the diffusive flux in the near-wall region (Trujillo et al., 2009).

$$J_{i,w} = \frac{\mu_{\mathrm{T,\ layer}}}{S_{\mathrm{c,T}}}\nabla Y_i \tag{29}$$

Where $\bigtriangledown Y_i$ represents the mass fraction of corrosive medium i in solution. $\mu_{\mathrm{T,layer}}$ is the turbulent viscosity (Wolfshtein, 1969):

$$\mu_{\mathrm{T,layer}} = \rho C_\mu l_\mu \sqrt{k} \tag{30}$$

Substituting Eq. (30) into Eq. (29) and associating it with Eqs. (27) and (28), gives:

$$\left(\frac{1}{\kappa}\ln y^+ + 5.5 + P_c\right)\cdot \nabla Y_i \cdot \rho C_\mu^{3/4}\cdot l_\mu = (C_{i,w} - C_i) \tag{31}$$

Higher v_{rs} (exceeding the $Re_{,c}$) tends to produce a magnified concentration gradient at a given wall distance y^+. The enhanced concentration gradient of the corrosive medium in the viscous sublayer and the increased contact frequency between Ca^{2+} and CO_3^{2-} in solution promote the nucleation and growth of carbonate crystals (Gao et al., 2011). There is significant variability in the corrosion mechanisms occurring at different flow regimes, as depicted in Figs. 17 and 18. The unimpeded and intensified mass transfer facilitated by the vortex at 80 °C induces an augmented corrosion effect. Consequently, the nucleation of $CaCO_3$ crystals assumes a dominant role in the scale deposition process. However, the situation is somewhat different at 150 °C, as dual effects are observed at elevated v_{rs}: firstly, the vortex cell structure is disrupted, and secondly, the densification of the inner $FeCO_3$ scale layer is notably enhanced, which impedes corrosion.

5. Conclusion

The corrosion behavior and evolution of the corrosion scale of N80 steel in high temperature and high pressure and high-mineralization (HTHP) oilfield-produced water systems under different flow regimes were investigated using HTHP corrosion weightlessness tests and surface characterization techniques at 80

and 150 °C. Different flow regimes, including stationary, laminar, and turbulent flow, are simulated by changing the rotational speed (v_{rs}) within the reactor. Conclusions can be drawn.

- The corrosion rate is significantly influenced by the flow regimes. At 80 °C, the corrosion rate increases linearly with the v_{rs}. At 150 °C, the corrosion rate reaches a maximum value at 300 rpm and subsequently decreases. Combined with the Gumbel probability distribution plot, increasing v_{rs} and temperature can promote the expansion of the pitting area and pitting depth. Hence, elevated temperature and v_{rs} are crucial factors in the initiation and propagation of localized corrosion.
- Temperature induces the corrosion scale conversion of aragonite $CaCO_3$ (80 °C) to calcite (150 °C). The protective properties of corrosion scales consisting of calcite $CaCO_3$ with an inner layer of $FeCO_3$ at 150 °C were found to be superior to those composed of dendritic aragonite $CaCO_3$ with an inner layer of Fe_3C at 80 °C. Furthermore, nucleation processes predominantly govern the formation of aragonite $CaCO_3$ crystals, whereas growth processes dominate the development of calcite $CaCO_3$.
- The vortex structure in the flow field significantly influences the corrosion scale and mass transfer processes in the reactor. The homogeneous vortex cells with low Re at 80 °C enhance the mass transfer processes. However, at 150 °C, the vortex cell structure is destroyed as the v_{rs} increases to 300 rpm and exceeds the critical rotational Reynolds number (63669.44), resulting in viscous dissipation that inhibits mass transfer and reduces the corrosion rate.

CRediT authorship contribution statement

Liu-Yang Yang: Writing – review & editing, Writing – original draft, Visualization, Validation, Software, Project administration, Methodology, Investigation, Formal analysis, Data curation, Conceptualization. **Chang-Pu Liu:** Resources, Investigation, Formal analysis, Data curation, Conceptualization. **Hai-Ming Fan:** Writing – original draft, Visualization, Project administration, Methodology, Investigation, Funding acquisition, Formal analysis, Data curation, Conceptualization. **Da-Lei Zhang:** Visualization, Supervision, Resources, Project administration, Funding acquisition, Formal analysis, Data curation, Conceptualization. **Zhi-Yi Wei:** Investigation, Formal analysis, Data curation. **Hui-Liang Wu:** Methodology, Investigation, Formal analysis, Data curation. **Chuan He:** Project administration, Data curation, Conceptualization. **Ye-Fei Wang:** Methodology, Investigation, Funding acquisition.

Declaration of competing interest

The authors declare that they have no known competing financial interests or personal relationships that could have appeared to influence the work reported in this paper.

Acknowledgment

This work was supported by the National Natural Science Foundation in China (52434002, 42176209, 52074339), the Natural Science Foundation of Shandong Province (ZR2021ME007) and the Opening Fund of Shandong Key Laboratory of Oilfield Chemistry and the Fundamental Research Funds for the Central Universities (19CX05006A).

Appendix A. Supplementary data

Supplementary data to this article can be found online at https://doi.org/10.1016/j.petsci.2024.11.002.

References

Akeer, E.S., 2014. Effect of Carbon Steel Composition and Microstructure on CO_2 Corrosion. Ohio University.
Alaba, P.A., Adedigba, S.A., Olupinla, S.F., Agboola, O., Sanni, S.E., 2020. Unveiling corrosion behavior of pipeline steels in CO_2-containing oilfield produced water: towards combating the corrosion curse. Crit. Rev. Solid State Mater. Sci. 45 (3), 239–260. https://doi.org/10.1080/10408436.2019.1588706.
Al-Hassan, S., Mishra, B., Olson, D.L., Salama, M.M., 1998. Effect of microstructure on corrosion of steels in aqueous solutions containing carbon dioxide. Corrosion 54 (6), 480–491. https://doi.org/10.5006/1.3284876.
Alsaiari, H., Kan, A., Tomson, M., 2009. Molar ratio of Ca^{2+} to Fe^{2+} in the supersaturated solution of iron carbonate and calcium carbonate and in the precipitate: relation and interpretation. SPE Int. Symp. Oilfield Chem. 57 (1), 207–214. https://doi.org/10.2118/121553-MS.
Alsaiari, H.A., Kan, R., Tomson, R.B., 2010a. Effect of calcium and iron (II) ions on the precipitation of calcium carbonate and ferrous carbonate. SPE J. 15 (2), 294–300. https://doi.org/10.2118/121553-pa.
Alsaiari, H.A., Tomson, M.B., Kan, A.T., 2010b. Constant Composition study of crystal growth of mixed calcium-ferrous carbonate salt. NACE-Int. Corros. Conf. Ser 10130.
Alwis, C.D., Trought, M., Lundeen, J., Perrine, K.A., 2021. Effect of cations on the oxidation and atmospheric corrosion of iron interfaces to minerals. J. Phys. Chem. A. 125 (36), 8047–8063. https://doi.org/10.1021/acs.jpca.1c06451.
Azzolina, N.A., Nakles, D.V., Gorecki, C.D., Peck, W.D., Ayash, S.C., Melzer, L.S., Chatterjee, S., 2015. CO_2 storage associated with CO_2 enhanced oil recovery: a statistical analysis of historical operations. Int. J. Greenh. Gas Control 37, 384–397. https://doi.org/10.1016/j.ijggc.2015.03.037.
Azzolina, N.A., Peck, W.D., Hamling, J.A., Gorecki, C.D., Ayash, S.C., Doll, T.E., Nakles, D.V., Melzer, L.S., 2016. How green is my oil? A detailed look at greenhouse gas accounting for CO_2-enhanced oil recovery (CO_2-EOR) sites. Int. J. Greenh. Gas Control 51, 369–379. https://doi.org/10.1016/j.ijggc.2016.06.008.
Balestrin, E., Arruda Guelli Ulson de Souza, S.M., Valle, J.A.B., da Silva, A., 2021. Sensitivity of the turbulent Schmidt number and the turbulence models to simulate catalytic and photocatalytic processes with surface reaction limited by mass transfer. Chem. Eng. Res. Des. 170 (1), 90–106. https://doi.org/10.1016/j.cherd.2021.03.035.
Bénézeth, P., Dandurand, J.L., Harrichoury, J.C., 2009. Solubility product of siderite ($FeCO_3$) as a function of temperature (25–250 °C). Chem. Geol. 265, 3–12. https://doi.org/10.1016/j.chemgeo.2009.03.015.
Bénézeth, P., Saldi, G.D., Dandurand, J.L., Schott, J., 2011. Experimental determination of the solubility product of magnesite at 50 to 200 °C. Chem. Geol. 286 (1–2), 21–31. https://doi.org/10.1016/j.chemgeo.2011.04.016.
Chen, S.S., Wang, H.X., Jiang, H., Liu, Y.N., Liu, Y.X., Lv, X.X., 2021. Risk assessment of corroded casing based on analytic hierarchy process and fuzzy comprehensive evaluation. Petrol. Sci. 18, 591–602. https://doi.org/10.1007/s12182-020-00507-0.
Chen, M., Zhang, Y., Liu, S., Zhao, C., Dong, S., Song, Y., 2023. CO_2 transport and carbonate precipitation in the coupled diffusion-reaction process during CO_2 storage. Fuel 334, 126805. https://doi.org/10.1016/j.fuel.2022.126805.
Crolet, J.L., Thevenot, N., Nesic, S., 1996. Role of conductive corrosion products on the protectiveness of corrosion layers. Corrosion 54 (3), 194–203. https://doi.org/10.5006/1.3284844.
Davoodi, S., Al-Shargabi, M., Wood, D.A., Rukavishnikov, V.S., Minaev, K.M., 2023. Review of technological progress in carbon dioxide capture, storage, and utilization. Gas Sci. Eng. 117, 205070. https://doi.org/10.1016/j.jgsce.2023.205070.
Dorange, G., Marchand, A., Guyader, M.L., 2005. Calcite solubility product and dissociation constants of $CaHCO_3^+$ and $CaCO_3^0$ between 5 and 75 °C. J. Water Sci. 3 (3), 261–275. https://doi.org/10.7202/705074ar.
Drela, I., Falewicz, P., Kuczkowska, S., 1998. New rapid test for evaluation of scale inhibitors. Water Res. 32, 3188–3191. https://doi.org/10.1016/s0043-1354(98)00066-9.
Elgaddafi, R., Ahmed, R., Shah, S., 2021. The effect of fluid flow on CO_2 corrosion of high-strength API carbon steels. J. Nat. Gas Sci. Eng. 86, 103739. https://doi.org/10.1016/j.jngse.2020.103739.
Esmaeely, S.N., Choi, Y.S., Young, D., Nesic, S., 2013. Effect of calcium on the formation and protectiveness of iron carbonate layer in CO_2 corrosion. Corrosion 69 (9), 6310–6327. https://doi.org/10.5006/0942.
Gao, M., Pang, X., Gao, K., 2011. The growth mechanism of CO_2 corrosion product films. Corrosion Sci. 53, 557–568. https://doi.org/10.1016/j.corsci.2010.09.060.
Gu, H., Chen, Y., Wu, J., Jiang, Y., Sundén, B., 2021. Impact of discharge port configurations on the performance of sliding vane rotary compressors with a rotating cylinder. Appl. Therm. Eng. 186, 116526. https://doi.org/10.1016/j.applthermaleng.2020.116526.
Guo, S., Xu, L., Zhang, L., Chang, W., Lu, M., 2012. Corrosion of alloy steels containing 2% chromium in CO_2 environments. Corrosion Sci. 63, 246–258. https://doi.org/10.1016/j.corsci.2012.06.006.
Han, J., Young, D., Colijn, H., Tripathi, A., Nesic, S., 2009. Chemistry and structure of

the passive film on mild steel in CO_2 corrosion environments. Ind.eng.chem.res. 48, 6296–6302. https://doi.org/10.1021/ie801819y.
Hua, Y., Shamsa, A., Barker, R., Neville, A., 2018. Protectiveness, morphology and composition of corrosion products formed on carbon steel in the presence of Cl^-, Ca^{2+} and Mg^{2+} in high pressure CO_2 environments. Appl. Surf. Sci. 455, 667–682. https://doi.org/10.1016/j.apsusc.2018.05.140.
Ishaq, H., Crawford, C., 2023. CO_2-based alternative fuel production to support development of CO_2 capture, utilization and storage. Fuel 331, 125684. https://doi.org/10.1016/j.fuel.2022.125684.
Jones, B., 2017. Review of aragonite and calcite crystal morphogenesis in thermal spring systems. Sediment. Geol. 354, 9–23. https://doi.org/10.1016/j.sedgeo.2017.03.012.
Jones, B., Peng, X., 2014. Hot spring deposits on a cliff face: a case study from Jifei, Yunnan Province, China. Sediment. Geol. 302, 1–28. https://doi.org/10.1016/j.sedgeo.2013.12.009.
Kontturi, K., Murtomki, L., Manzanares, J.A., 2008. Ionic Transport Processes. Oxford University Press.
Li, G.J., Zhang, J., 2011. Progress and implications of carbon dioxide capture and geological storage projects. Sino–Global Energy 16 (6), 12–16.
Li, X., Zhao, Y., Qi, W., Xie, J., Wang, J., Liu, B., Zeng, G., Zhang, T., Wang, F., 2019. Effect of extremely aggressive environment on the nature of corrosion scales of HP–13Cr stainless steel. Appl. Surf. Sci. 469, 146–161. https://doi.org/10.1016/j.apsusc.2018.10.237.
Lu, M., 2008. Effect of Alloying Elements and Microstructure on Steel Corrosion Behavior in CO_2 Environments, vol. 28, pp. 246–250.
Marosek, K.W., Christy, J.R.E., Macleod, N., Williamson, S., 1993. Development of a concurrent liquid-liquid core—annular flow column to prevent wall deposition in coagulation studies. Chem. Eng. Sci. 48, 1061–1068.
Masuda, H., Shimoyamada, M., Ohmura, N., 2019. Heat transfer characteristics of Taylor vortex flow with shear–thinning fluids. Int. J. Heat Mass Tran. 130, 274–281. https://doi.org/10.1016/j.ijheatmasstransfer.2018.10.095.
Navabzadeh, S., Young, D., Brown, B., Nesic, S., 2016. Effect of incorporation of calcium into iron carbonate protective layers in CO_2 corrosion of mild steel. Corrosion 73 (3), 238–246. https://doi.org/10.5006/2261.
Neerup, R., Løge, I.A., Kontogeorgis, G.M., Thomsen, K., Fosbøl, P.L., 2023. Measurements and modelling of $FeCO_3$ solubility in water relevant to corrosion and CO_2 mineralization. Chem. Eng. Sci. 270, 118549. https://doi.org/10.1016/j.ces.2023.118549.
Nešsić, V.R.M.V.S., 2006. Protective iron carbonate films–Part 2: chemical removal by dissolution in single–phase aqueous flow. Corrosion 62 (7), 598–611. https://doi.org/10.5006/1.3280674.
Neville, Anne, Barker, Richard, Pessu, Frederick, 2015. The influence of pH on localized corrosion behavior of X65 carbon steel in CO_2–saturated brines. Corrosion J. Sci. Eng. 71 (12), 1452–1466. https://doi.org/10.5006/1770.
Ochoa, N., Vega, C., Pébère, N., Lacaze, J., Brito, J.L., 2015. CO_2 corrosion resistance of carbon steel in relation with microstructure changes. Mater. Chem. Phys. 156, 198–205. https://doi.org/10.1016/j.matchemphys.2015.02.047.
Owen, J., Ropital, F., Joshi, G.R., Kittel, J., Barker, R., 2022. Galvanic effects induced by siderite and cementite surface layers on carbon steel in aqueous CO2 environments. Corrosion Sci. 209, 110762. https://doi.org/10.1016/j.corsci.2022.110762.
Owen, J., Burkle, D., Joshi, G.R., Basilico, E., Kittel, J., Ropital, F., Marcelin, S., Kleppe, A., Woollam, R.C., Barker, R., 2023. In situ SR–XRD analysis of corrosion product formation during 'pseudo–passivation' of carbon steel in CO_2–containing aqueous environments. Corrosion Sci. 225, 111598. https://doi.org/10.1016/j.corsci.2023.111598.
Paolinelli, L.D., Carr, G.E., 2015. Mechanical integrity of corrosion product films on rotating cylinder specimens. Corrosion Sci. 92, 155–161. https://doi.org/10.1016/j.corsci.2014.11.042.
Paolinelli, L.D., Nesic, S., 2021. Calculation of mass transfer coefficients for corrosion prediction in two- phase gas–liquid pipe flow. Int. J. Heat Mass Tran. 165, 120689. https://doi.org/10.1016/j.ijheatmasstransfer.2020.120689.
Ren, X., Wang, H., Wei, Q., Lu, Y., Xie, J., 2021. Electrochemical behaviour of N80 steel in CO_2 environment at high temperature and pressure conditions. Corrosion Sci. 189, 109619. https://doi.org/10.1016/j.corsci.2021.109619.
Rivero, E.P., Granados, P., Rivera, F.F., Cruz, M., González, I., 2010. Mass transfer modeling and simulation at a rotating cylinder electrode (RCE) reactor under turbulent flow for copper recovery. Chem. Eng. Sci. 65, 3042–3049. https://doi.org/10.1016/j.ces.2010.01.030.
Rizzo, R., Gupta, S., Rogowska, M., Ambat, R., 2020. Corrosion of carbon steel under CO_2 conditions: effect of $CaCO_3$ precipitation on the stability of the $FeCO_3$ protective layer. Corrosion Sci. 162, 108214. https://doi.org/10.1016/j.corsci.2019.108214.
Ruzic, V., Veidt, M., Nesic, S., 2006. Protective iron carbonate films–Part 1: mechanical removal in single-phase aqueous flow. Corrosion 62 (5), 598–611. https://doi.org/10.5006/1.3278279.
Ruzic, V., Veidt, M., Nesic, S., 2007. Protective Iron Carbonate Films–Part 3: simultaneous chemo-mechanical removal in single-phase aqueous flow. Corrosion 63 (8), 758–769. https://doi.org/10.5006/1.3278425.
Shamsa, A., Barker, R., Hua, Y., Barmatov, E., Neville, A., 2019. The role of Ca^{2+} ions on Ca/Fe carbonate products on X65 carbon steel in CO_2 corrosion environments at 80 and 150 °C. Corrosion Sci. 156. https://doi.org/10.1016/j.corsci.2019.05.006.
Shih, T.H., Liou, W.W., Shabbir, A., Yang, Z., Zhu, J., 1995. A new k–ϵ eddy viscosity model for high Reynolds number turbulent flows. Comput. Fluids 24, 227–238. https://doi.org/10.1016/0045-7930(94)00032-t.
Speziale, C.G., Thangam, S., 1992. Analysis of an RNG based turbulence model for separated flows. Int. J. Eng. Sci. 30, 1379–1388. https://doi.org/10.1016/0020-7225(92)90148-A.
Tan, Z., Yang, L., Zhang, D., Wang, Z., Cheng, F., Zhang, M., Jin, Y., 2020. Development mechanism of internal local corrosion of X80 pipeline steel. J. Mater. Sci. Technol. 49, 186–201. https://doi.org/10.1016/j.jmst.2019.10.023.
Theodorsen, T., Regier, A., 1944. Experiments on drag of revolving disks, cylinders and streamline rods at high speeds. Geology 37 (12), 1059–1062. https://doi.org/10.1130/G30448A.1.
Trujillo, F.J., Safinski, T., Adesina, A.A., 2009. Solid–liquid mass transfer analysis in a multi–phase tank reactor containing submerged coated inclined–plates: a computational fluid dynamics approach. Chem. Eng. Sci. 64, 1143–1153. https://doi.org/10.1016/j.ces.2008.11.004.
Wang, Y., Wang, B., Xing, X., He, S., Zhang, L., Lu, M., 2022a. Effects of flow velocity on the corrosion behaviour of super 13Cr stainless steel in ultra–HTHP CO_2–H_2S coexistence environment. Corrosion Sci. 200, 110235. https://doi.org/10.1016/j.corsci.2022.110235.
Wang, Z., Zhao, Y., Liu, M., Shen, H., Fang, Q., Yao, J., 2022b. Investigation of the effects of small flow rate and particle impact on high temperature CO_2 corrosion of N80 steel. Corrosion Sci. 209, 110735. https://doi.org/10.1016/j.corsci.2022.110735.
Wang, C.L., Guo, H.D., Fang, J., Yu, S.X., Yue, X.Q., Hu, Q.H., Liu, C.W., Zhang, J.X., Zhang, R., Xu, X.S., Hua, Y., Li, Y.X., 2023. The role of Cr content on the corrosion resistance of carbon steel and low-Cr steels in the CO_2–saturated brine. Petrol. Sci. 20, 1155–1168. https://doi.org/10.1016/j.petsci.2022.11.016.
Wei, J., Dong, J., Zhou, Y., He, X., Wang, C., Ke, W., 2018. Influence of the secondary phase on micro galvanic corrosion of low carbon bainitic steel in NaCl solution. Mater. Char. 139, 401–410. https://doi.org/10.1016/j.matchar.2018.03.021.
Weigand, B., Ferguson, J.R., Crawford, M.E., 1997. An extended Kays and Crawford turbulent Prandtl number model. Int. J. Heat Mass Tran. 40, 4191–4196. https://doi.org/10.1016/s0017-9310(97)00084-7.
Wolfshtein, M., 1969. The velocity and temperature distribution in one-dimensional flow with turbulence augmentation and pressure gradient. Int. J. Heat Mass Tran. 12, 301–318. https://doi.org/10.1016/0017-9310(69)90012-x.
Yan, W., Wei, H.G., Muchiri, N.D., Li, F.L., Zhang, J.R., Xu, Z.X., 2023. Degradation of chemical and mechanical properties of cements with different formulations in CO_2–containing HTHP downhole environment. Petrol. Sci. 20, 1119–1128. https://doi.org/10.1016/j.petsci.2023.03.012.
Yang, Y., Brown, B., Nei, S., Gennaro, M., Molinas, B., 2010. Mechanical strength and removal of a protective iron carbonate layer formed on mild steel in CO_2 corrosion. NACE-Int. Corros. Conf. Ser. 10383. https://www.researchgate.net/publication/241793223.
Yang, L., Zhang, D., Fan, H., Tan, Z., Xing, S., Guan, X., Jiang, X., 2022. Investigating the micro–turbulent corrosion mechanism of pipeline defects based on a combined experimental and simulation approach. J. Nat. Gas Sci. Eng. 106, 104745. https://doi.org/10.1016/j.jngse.2022.104745.
Yang, Z., Zhao, M., Bi, W., Cheng, Y., Ma, Z., Liu, K., Li, Y., Dai, C., 2024. Synthesis and analysis of drag reduction performance of the temperature–resistant polymer slickwater for high temperature reservoirs. J. Mol. Liq. 397, 124137. https://doi.org/10.1016/j.molliq.2024.124137.
Ye, L., Wan, T., Xie, X., Hu, L., 2022. Study on flow characteristics and mass transfer mechanism of kettle taylor flow reactor. Energies 15 (6), 1–16. https://doi.org/10.3390/en15062028.
Yin, Z.F., Feng, Y.R., Zhao, W.Z., Bai, Z.Q., Lin, G.F., 2009. Effect of temperature on CO_2 corrosion of carbon steel. Surf. Interface Anal. 41, 517–523. https://doi.org/10.1002/sia.3057.
Yue, X.Q., Zhang, L., Ma, L., Lu, M.X., Neville, A., Hua, Y., 2020. Influence of a small velocity variation on the evolution of the corrosion products and corrosion behaviour of super 13Cr SS in a geothermal CO_2 containing environment. Corrosion Sci. 178, 108983. https://doi.org/10.1016/j.corsci.2020.108983.
Zhang, D.L., Yang, L.Y., Tan, Z.W., et al., 2021. Corrosion behavior of X65 steel at different depths of pitting defects under local flow conditions. Exp. Therm. Fluid Sci. 124, 110333. https://doi.org/10.1016/j.expthermflusci.2020.110333.
Zhao, Y.L., Ye, F.X., Zhang, G., Yao, J., Liu, Y.F., Dong, S.G., 2022. Investigation of erosion–corrosion behavior of Q235B steel in liquid–solid flows. Petrol. Sci. 19, 2358–2373. https://doi.org/10.1016/j.petsci.2022.05.020.